

UC Irvine

UC Irvine Previously Published Works

Title

Revealing the Influence of Binding Motifs on Electron Transfer and Recombination Kinetics for CdSe Quantum Dots Functionalized with a Modified Viologen

Permalink

<https://escholarship.org/uc/item/3p886410>

Authors

Bird, Olivia F

Drbohlav, Kenneth M

Gowdy, Evan K

et al.

Publication Date

2025

DOI

10.1021/acs.jpcc.5c00740

Supplemental Material

<https://escholarship.org/uc/item/3p886410#supplemental>

Copyright Information

This work is made available under the terms of a Creative Commons Attribution License, available at <https://creativecommons.org/licenses/by/4.0/>

Peer reviewed

Revealing the Influence of Binding Motifs on Electron Transfer and Recombination Kinetics for CdSe Quantum Dots Functionalized with a Modified Viologen

Olivia F. Bird, Kenneth M. Drbohlav,  Evan K. Gowdy,  Faith A. Flinkingshelt, Lauren M. Pellows, Benjamin F. Hammel, Bradley W. Layne, Shane Ardo, Jenny Y. Yang, Kenneth A. Miller, and Gordana Dukovic*

 Cite This: <https://doi.org/10.1021/acs.jpcc.5c00740>

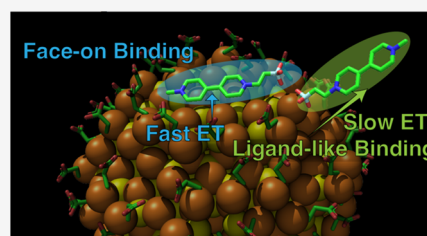
ACCESS |

 Metrics & More

|  Article Recommendations

|  Supporting Information

ABSTRACT: Anchoring of molecules to the surfaces of semiconductor nanocrystals (NCs) presents an opportunity to leverage the precise synthetic tunability of molecular function and the remarkable light harvesting properties of NCs to drive photochemical reactions. However, charge transfer between the two species depends not only on the energy level alignments but also on the details of their binding interactions, which are difficult to probe. Here, we characterize the binding between CdSe quantum dots (QDs) and a new phosphonated derivative of the electron acceptor methyl viologen, designed to attach to the QD surface via the phosphonate group. We use isothermal titration calorimetry to probe the thermodynamics of the QD–molecule interaction and use the parameters determined therein to analyze transient absorption spectroscopy measurements of forward and back electron transfer from QDs to the viologen. We find that the ligand-like phosphonate binding leads to an electron-transfer rate constant that is 3 orders of magnitude smaller than that for the face-on binding of the bipyridine ring of methyl viologen. Back electron transfer is also significantly slower in the derivative. Interestingly, a minor fraction of the phosphonated derivative also binds in the face-on configuration, with similar forward and back electron transfer kinetics as methyl viologen. Numerical simulations show that the ligand-like binding will lead to significantly improved quantum yields of photocatalysis over a wide range of reaction rates. By independently characterizing binding thermodynamics and charge transfer kinetics, this work reveals how the complexities underlying electron transfer at the NC–molecule interface determine photocatalytic outcomes. This work also represents a step toward controlling forward and back electron transfer kinetics via rational molecular design.



INTRODUCTION

Hybrid materials consisting of semiconductor nanocrystals (NCs) with bound molecular species leverage the remarkable light-harvesting properties of NCs with the atomically precise control of molecules to tune their function.^{1–5} In particular, NCs have been functionalized with a variety of molecular electron acceptors and reduction catalysts with the aim of converting photon energy into reduced chemical products.^{1,2,6–11} In these systems, electron transfer (ET) from photoexcited NCs to the molecular species competes with electron–hole recombination and electron trapping.^{2–5} Once transferred, electrons may recombine with holes via back electron transfer (BET) before they turn over in a catalytic reaction. To spontaneously drive desired reactions with light, ET and BET need to be optimized so that charge separation is sufficiently efficient to generate the charge-separated state and charge recombination is sufficiently slow to allow catalysis to proceed.

In principle, the tools of synthetic chemistry can be used to design electron acceptors with fine-tuned rates of ET and BET by incorporating targeted binding groups for NC surfaces and

varying the chemical nature of the spacer between the binding group and the electron accepting moiety. In practice, there are fundamental obstacles to realizing the ideal scenarios for specific photocatalytic reactions. The first obstacle is the complexity of the NC surfaces, decorated with surface-capping ligands that induce solubility in a limited range of solvents. When combined with NCs, molecules designed to control charge transfer kinetics do not always behave as designed. For example, when a common electron acceptor methyl viologen (MV^{2+}) was functionalized with different aliphatic chain length tails, ET rate constants (k_{ET}) remained essentially the same because MV^{2+} adheres strongly to the NC surface, creating a direct through-space ET channel.¹² In other cases, acceptor adsorption relies on the precipitation of insoluble molecules

Received: January 31, 2025

Revised: February 14, 2025

Accepted: February 18, 2025

onto the NC surface with limited chemical control.^{13–16} A second obstacle is the challenge of revealing the binding geometries, identifying underlying adsorption modes, and characterizing binding thermodynamics to determine the number of acceptors bound per NC. NMR has been proven useful in specific cases,^{17–21} but it requires well-suited signals with optimal binding-induced peak broadening as well as high sample volumes.^{22,23} The binding challenge is compounded by the fact that acceptor adsorption is inherently convoluted with ET (i.e., more acceptors bound leads to faster ET rates for the same k_{ET}). Spectroscopic measurements of ET kinetics using time-resolved spectroscopy detect ET as a shortening of the kinetics of signals attributed to conduction-band electrons.^{5,12,24–33} Kinetic models that extract k_{ET} values and the number of acceptors bound have been developed and used^{5,15,22,28,33,34} but they rely on assumptions about binding that are not easily independently verified. Moreover, there is a mathematical correlation of k_{ET} values and the number of acceptors bound, creating uncertainties in both values.^{22,34–36} Finally, there is an obstacle in balancing the roles of ET and BET in overall photocatalysis. This can be particularly difficult as certain factors that facilitate faster ET, such as strong electronic coupling, also facilitate fast BET.³⁷ While unity charge separation efficiency has been achieved in multiple systems,^{37–40} it is not necessarily beneficial if the charge-separated state is not long-lived enough to support turnover. While it is generally accepted that both fast ET and slow BET are desirable, little guidance has emerged on how to balance these requirements to maximize the efficiencies of subsequent reactions.

In this article, we address these obstacles with CdSe quantum dots (QDs) functionalized with a new phosphonated viologen derivative (MVPO₃, illustrated in Figure 1), which we

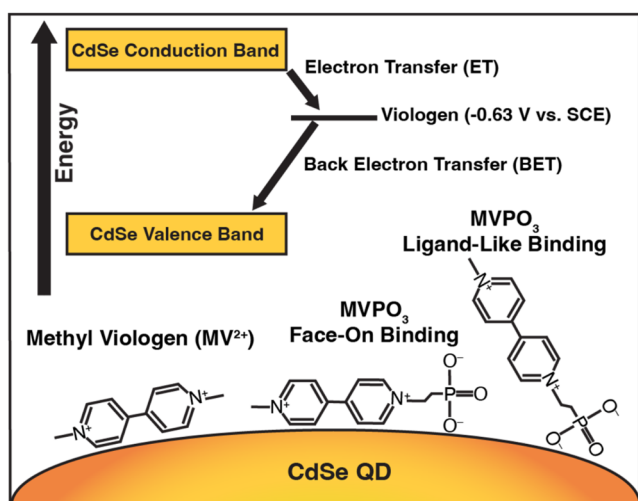


Figure 1. Energy level diagram and illustration of binding modes for CdSe QDs functionalized with MV²⁺ and MVPO₃.

compare to QDs functionalized with the familiar MV²⁺. The phosphonate terminal group on the derivative was introduced to guide the anchoring to the CdSe QD surface so that the rate constants for ET and BET could be governed by the moiety bridging the anchoring group and the bipyridine group that accepts the electron. We first characterized QD–acceptor binding by using isothermal titration calorimetry (ITC), which allowed us to determine thermodynamic parameters, including

the dissociation equilibrium constant (K_d) and the maximum number of acceptors that can bind (n_{max}), for both MV²⁺ and MVPO₃. We validated our ITC approach with MV²⁺ and QDs, characterizing the previously described “face-on” binding mode. Remarkably, the ITC data on MVPO₃ attachment to the QDs resolved two distinct binding modes: a minor one with thermodynamics similar to MV²⁺ binding, which we attributed to analogous face-on binding, and a major mode, which we assigned to the phosphonate binding (Figure 1). The ITC measurements informed our subsequent transient absorption (TA) spectroscopy measurements of charge transfer kinetics. Specifically, we used the information from the ITC measurements as inputs into the models for the TA decay kinetics, allowing us to determine the values of k_{ET} associated with each binding mode as the only adjustable parameters in the data fitting. We revealed two distinct k_{ET} values for ET from QDs to MVPO₃, one similar to MV²⁺ ($1.5 \times 10^{10} \text{ s}^{-1}$) associated with the face-on binding and another much slower ($3.0 \times 10^7 \text{ s}^{-1}$) associated with phosphonate binding. We also spectroscopically examined the BET reaction and found that the phosphonated derivative had a >30-fold increase in charge-separated-state lifetime as compared to MV²⁺. In other words, the new binding mode in MVPO₃ slowed down both ET and BET when compared with MV²⁺. To assess the impact of this effect on photocatalysis, we used kinetic Monte Carlo (kMC) simulations to determine the quantum yield (QY) of a hypothetical downstream reaction that uses the electrons transferred to the bipyridine moiety. We identified a broad regime of downstream reaction rate constants ($10^3\text{--}10^7 \text{ s}^{-1}$) where the ET/BET combination achieved with MVPO₃ significantly outperforms MV²⁺. This work demonstrates how the complexities of binding of molecules to semiconductor NCs and their impact on photocatalysis can be revealed by independently characterizing binding and interfacial charge transfer. Our work also represents a step forward in controlling ET and BET kinetics in NC–molecule systems via rational molecular design.

METHODS

MVPO₃ Synthesis and Characterization. *General Experimental Procedures.* All chemicals were purchased from Sigma-Aldrich and used without further purification. All solvents were degassed with N₂ and passed through activated molecular sieves prior to use. Reactions involving air or moisture sensitive reagents or intermediates were performed under an inert N₂ atmosphere using glassware that had been oven or flame-dried. The ¹H and ¹³C NMR spectra were obtained on a Bruker Avance NEO-400 spectrometer, operating at 400 and 100 MHz, respectively.

*1-(2-(Diethoxyphosphoryl)ethyl)-[4,4'-bipyridin]-1-ium Bromide (1).*⁴¹ A solution of 4,4'-dipyridyl (2.0 g, 12.8 mmol) and 2-bromoethyl diethylphosphonate (1.54 g, 1.14 mL, 6.2 mmol) in CH₃CN (20 mL) was heated to 50 °C for 48 h. The solution was concentrated under reduced pressure and suspended in acetone (20 mL) and stirred for 1 h. The solid was filtered washing with acetone (2 × 20 mL) to give 1.3 g (66%) of a beige solid; ¹H NMR (400 MHz, D₂O) δ 8.97 (d, *J* = 6.4 Hz, 2 H), 8.71 (d, *J* = 6.0 Hz, 2 H), 8.40 (d, *J* = 6.4 Hz, 2 H), 7.86 (d, *J* = 6.0 Hz, 2 H), 4.90 (dt, *J* = 17.6, 6.8 Hz, 2 H), 4.04 (m, 4 H), 2.72 (dt, *J* = 18.4, 6.8 Hz, 2 H), 1.16 (t, *J* = 7.2 Hz, 6 H); ¹³C NMR (100 MHz, D₂O) δ 154.6, 150.0, 145.3, 142.3, 126.1, 122.5, 63.9 (d, *J*_{P,C} = 6.0 Hz), 55.4 (d, *J*_{P,C} = 5.0 Hz), 26.0 (d, *J*_{P,C} = 141 Hz) 15.5 (d, *J*_{P,C} = 5.0 Hz); IR (neat)

cm^{-1} 3467, 2988, 1642, 1545, 1525, 1407, 1242, 1210, 1010, 972, 815, 689; HRMS (ESI-TOF) m/z 321.1373 [$\text{C}_{16}\text{H}_{22}\text{N}_2\text{O}_3\text{P}^+$ (M^+) requires 321.1368].

1-(2-(Diethoxyphosphoryl)ethyl)-1'-methyl-[4,4'-bipyridine]-1,1'-dium Dibromide (2). A mixture of diethyl phosphonate **1** (478 mg, 1.2 mmol) and CH_3I (341 mg, 0.15 mL, 2.4 mmol) in CH_3CN (5 mL) was heated to 50 °C for 3 h, and additional CH_3I (341 mg, 0.15 mL, 2.4 mmol) was added. The mixture was stirred at 50 °C for 24 h and cooled to room temperature. The solid was filtered washing with CH_3CN (2×10 mL) to give 354 mg (54%) of an orange solid; ^1H NMR (400 MHz, D_2O) δ 9.13 (d, $J = 6.8$ Hz, 2H), 9.00 (d, $J = 6.8$ Hz, 2H), 8.55 (d, $J = 6.8$ Hz, 2H), 8.47 (d, $J = 6.4$ Hz, 2H), 4.97 (dt, $J = 16.8, 7.2$ Hz, 2H), 4.44 (s, 3H), 4.07 (m, 4H), 2.76 (dt, $J = 18.4, 7.2$ Hz, 2H), 1.19 (t, $J = 7.2$ Hz, 6H); ^{13}C NMR (100 MHz, D_2O) δ 150.9, 149.5, 146.4, 146.0, 127.2, 126.9, 64.1 (d, $J_{\text{P,C}} = 7.0$ Hz), 56.0 (d, $J_{\text{P,C}} = 4.0$ Hz), 48.6, 26.1 (d, $J_{\text{P,C}} = 141$ Hz), 15.6 (d, $J_{\text{P,C}} = 6.0$ Hz); IR (neat) cm^{-1} 3412, 2986, 1639, 1558, 1448, 1204, 1010, 943, 812, 706, 504; HRMS (ESI-TOF) m/z 336.1598 [$\text{C}_{17}\text{H}_{25}\text{N}_2\text{O}_3\text{P}^+$ (M^+) requires 336.1603].

1-Methyl-1'-(2-phosphonoethyl)-[4,4'-bipyridine]-1,1'-dium Dibromide (3, MVPO₃). A solution of viologen **2** (250 mg, 0.46 mmol) in 1 M HBr (17 mL) was heated to reflux for 24 h. The volume was then reduced to ca. 1 mL by boiling in the fume hood, and isopropyl alcohol (10 mL) was added. The resulting solid was filtered and washed with isopropyl alcohol (2×5 mL) to give 174 mg (86%) of an orange solid; ^1H NMR (400 MHz, D_2O) δ 9.10 (d, $J = 6.8$ Hz, 2H), 8.97 (d, $J = 6.8$ Hz, 2H), 8.48 (d, $J = 6.8$ Hz, 2H), 8.45 (d, $J = 6.8$ Hz, 2H), 4.87 (dt, $J = 12.4, 7.6$ Hz, 2H), 4.42 (s, 3H), 2.42 (dt, $J = 18.0, 7.6$ Hz, 2H); ^{13}C NMR (100 MHz, D_2O) δ 150.4, 149.8, 146.3, 145.6, 127.0, 126.7, 57.5, 48.4, 29.2 (d, $J_{\text{P,C}} = 133$ Hz); IR (neat) cm^{-1} 3338, 3036, 2739, 1634, 1500, 1089, 935, 808, 486; HRMS (ESI-TOF) m/z 279.0898 [$\text{C}_{13}\text{H}_{16}\text{N}_2\text{O}_3\text{P}^+$ (M^+) requires 279.0898].

Spectroelectrochemical Methods. Electronic absorption spectra were obtained on an Agilent Cary 60 ultraviolet–visible (UV–vis) spectrophotometer inside the glovebox under N_2 atmosphere using an Ocean Optics CUV 1.25 \times 1.25 \times 4.5 cm cuvette holder connected with an Agilent fiber optic coupler. The same spectrophotometer was used for spectroelectrochemical measurements with a Pine Wavedriver 10 bipotentiostat in a 1 \times 1 cm quartz cuvette. An Au screen-printed honeycomb electrode on a ceramic substrate with a thickness of 1.7 mm was used as the working and counter electrodes, and saturated KCl Ag/AgCl was used as the reference electrode. Spectroelectrochemical solutions contained aqueous 0.125 mM MV^{2+} or MVPO_3 in 0.25 M phosphate–NaOH buffer at pH 7.44.

Electrochemical Methods. Electrochemical measurements were conducted using a Pine Wavedriver 10 bipotentiostat under an inert N_2 atmosphere using standard glovebox or Schlenk line techniques. Cyclic voltammetry measurements were taken using a 3 mm carbon disk working electrode, a glassy carbon rod counter electrode, and a saturated KCl Ag/AgCl or SCE reference electrode, without correcting for IR compensation. The Ag/AgCl reference electrode was made according to published procedures.⁴² The working electrode was polished between each scan using an alumina slurry (0.05 mm) and a microcloth polishing pad, and washed with HPLC grade water in between scans. The phosphate buffer was made with HPLC grade water, monopotassium phosphate, and

NaOH. pH measurements were performed using a Thermo Scientific Orion Star A216 Benchtop pH/RDO/DO meter and a Thermo Scientific glass pH electrode 9142BN.

Synthesis and Purification of CdSe QDs. CdSe QDs were synthesized based on a previously published hot-injection synthesis.⁴³ The Se precursor was prepared by dissolving 0.183 g of elemental Se shot ($\geq 99\%$, Sigma-Aldrich) in 1.105 g tri-*n*-octylphosphine (TOP) ($\geq 97\%$, Strem Chemicals) under argon atmosphere. 0.062 g CdO ($\geq 99.99\%$, Sigma-Aldrich), 0.2814 g octadecylphosphonic acid (ODPA) ($\geq 99\%$, PCI Synthesis), and 3.0057 g of trioctylphosphine oxide (TOPO) ($\geq 99\%$, Sigma-Aldrich) were mixed in a round-bottom flask connected to a Schlenk line under argon. The solution was heated to 150 °C to melt the TOPO and the solution was placed under vacuum for 1 h. The solution was then put under Ar and heated to 300 °C until clear. We injected 1.500 g of TOP to the solution dropwise, which was then heated to 350 °C. Then, 0.4 mL of the Se:TOP precursor solution was injected and the particles were grown for 2 min before quenching by cooling in a room temperature oil bath. The particle solution was transferred to a vial containing 10 mL of methanol (99.8%, Sigma-Aldrich, anhydrous) under Ar atmosphere before transfer to an Ar glovebox. The QDs were then precipitated by centrifuging for 15 min at 3400 rpm and discarding the supernatant. Particles were resuspended in toluene (99.8%, Sigma-Aldrich, anhydrous), precipitated by methanol, and centrifuged at 3400 rpm for 15 min. The supernatant was discarded and the toluene/methanol wash was repeated. The particles were then redispersed in a minimal (<1 mL) volume of hexanes (99%, Sigma-Aldrich, anhydrous) and precipitated by the addition of 2-propanol (99.5%, Sigma-Aldrich, anhydrous) and centrifuged. The supernatant was discarded and the purified particles were then dispersed in 500 μL toluene.

CdSe QD Ligand Exchange. To suspend the CdSe QDs in H_2O , we carried out a ligand exchange from the native ODPA ligands to 3-mercaptopropionic acid (MPA) by modifying a previously described procedure.⁴⁴ The ligand exchange procedure was conducted in an Ar glovebox. A solution was prepared by dissolving 134 mg MPA ($\geq 99\%$, Sigma-Aldrich) and 316 mg of tetramethylammonium hydroxide (TMAH) ($\geq 97\%$, Sigma-Aldrich) in 15.004 g methanol. 2.00 mL of this solution was added to ca. 500 μL of the purified ODPA-capped CdSe QD stock in toluene. The solution turned optically clear within 2 min but was allowed to sit for 1.5 h to allow ample time for the ligand exchange to equilibrate. The ligand-exchanged particles were precipitated by adding 40 mL of toluene and centrifuging for 15 min at 4400 rpm. The supernatant was discarded and the resulting particles were resuspended in methanol, but the mixture was not optically clear upon resuspension. It was precipitated again with toluene and centrifuged for another 15 min at 4400 rpm. The particles did not fully precipitate (supernatant was still red). Thus, the supernatant solution was split into fourths, each fourth precipitated with an additional 30 mL of toluene and spun for 15 min at 4400 rpm. The resulting clear supernatant was removed from all four tubes, and the solid pellets were dried under vacuum for 30 min. The exchanged particles were then combined and dissolved in Milli-Q water.

Characterization of CdSe QDs. UV–vis absorbance data was collected using a Cary 60 UV–vis spectrophotometer (Agilent). Samples were prepared under Ar and sealed in 1 \times 1 cm air-free cuvettes. PL spectra were collected on a Fluorolog-

3 spectrofluorometer (Horiba Jobin Yvon). The PL sample was excited at 400 nm with a 3 nm slit width and PL was detected at 415–780 nm with a 3 nm slit width. Transmission electron microscopy (TEM) was performed with a FEI Tecnai G2 20 S-Twin operated at 200 kV. Samples were prepared in a glovebox by drop-casting MPA-capped CdSe QDs (diluted in methanol) onto TEM grids (Ted Pella, Prod # 01824, ultrathin carbon film on lacey carbon support film, 400 mesh, Cu). Grids were dried under vacuum and transported to the microscopy facility in an airtight container, sealed under the Ar atmosphere of the glovebox. The size of the QDs was measured using ImageJ (FIJI package) by manually fitting ellipsoids to the particle boundaries and recording the short axis of the ellipsoid as the diameter.⁴⁵ Measurements were performed on four different regions of the grid.⁴⁶

Isothermal Titration Calorimetry. Samples for ITC were prepared and stored under an Ar atmosphere before the experiment and were unavoidably exposed to air during the collection of ITC data. Samples were syringe-filtered using PTFE filters with 0.45 μm pore size (Thermo Scientific). ITC experiments were performed using a TA Instruments Affinity ITC Low Volume calorimeter with gold cells. As is standard procedure, the sample cell was overfilled past its 185 μL active volume with 29 μM CdSe QD in Milli-Q pure water. The reference cell was also filled with Milli-Q water. Viologen samples were prepared at 3.5 mM in Milli-Q water. The temperature was set to 25 $^{\circ}\text{C}$ and the samples were allowed to autoequilibrate for 30 min or until the baseline reached a slope of 0.1 $\mu\text{W}/\text{h}$ and standard deviation of 0.01 μW . Samples were stirred continuously at 150 rpm. Viologen samples were injected in $2.50 \pm 0.01 \mu\text{L}$ increments. Twenty injections were conducted, waiting until the peaks returned to baseline between injections (determined automatically by ITCRun software from TA Instruments with a minimum of 60 s between samples). The peaks were numerically integrated using the TA Instruments NanoAnalyze software to generate the isotherms. All titrations were run in triplicate to ensure reproducibility. All reported uncertainties of ITC fitting parameters are 95% confidence intervals of the best fits. Control titrations (solvent-into-solvent, viologen-into-solvent, and solvent-into-QD) were conducted at the same conditions as the relevant experimental titration. The integrated heat from the viologen-into-solvent controls were subtracted from the viologen-into-QD experimental data. The other controls had negligible signal (all peaks $< 1 \text{ kJ mol}^{-1}$).

Transient Absorption Spectroscopy. The ultrafast ($\sim 150 \text{ fs}$ to 7 ns) TA spectrometer used an amplified Ti:sapphire laser (Solstice-ACE, Spectra-Physics, 800 nm, 2 kHz, 150 fs, 1.8 mJ/pulse), an optical parametric amplifier (TOPAS-C, Light Conversion), and a Helios spectrometer (Ultrafast Systems, LLC). The Solstice output was split into a pump path and a probe path. The pump path was directed into the TOPAS-C to produce the 480 nm pump wavelength, which was then directed to the Helios spectrometer. CdSe QD-only data was taken at several powers and the pump power was chosen to be in the regime where the normalized decay kinetics were independent of power (i.e., negligible population of multiexcitons). The pump pulses were chopped by a 1000 Hz synchronized chopper before reaching the sample. The probe path was directed to a sapphire plate which converted the 800 nm light into a white light continuum from 450 to 800 nm. The probe beam was focused into the sample where it overlapped with the pump beam. The transmitted probe beam

was then passed through a polarization filter to remove residual scattered light from the pump beam and then focused into optical fibers coupled to multichannel spectrometers with CMOS sensors with 2 kHz detection rates. The change in absorbance signal (ΔA) was calculated from the intensities of sequential probe pulses with and without the pump pulse excitation. The 0.3 ns to 200 μs TA spectrometer used the amplified Ti:sapphire laser and optical parametric amplifier described above coupled with an Eos spectrometer (Ultrafast Systems, LLC). The pump–probe time delay was controlled by a digital delay generator (CNT-90, Pendulum Instruments). The white light continuum (400–900 nm) was generated for the probe signal and reference beams by an external 2 kHz laser focused into a photonic crystal fiber and split using a beam splitter. The probe and reference beams were focused into separate detectors. For all transient absorption measurements, the samples were sealed under Ar in 2 mm path length quartz cuvettes equipped with a Kontes valve and constantly stirred with a magnetic Teflon coated stir bar. CdSe QDs concentrations were kept constant at 10.6 μM and the viologen concentration was varied to achieve the desired ratios. All experiments were conducted at room temperature. The ultrafast and ns– μs kinetic traces were stitched together by normalizing the data between the two at a time point of overlap then removing all Eos data before that point and all Helios data after that point.

To analyze the kinetic traces from TA spectroscopy, we first isolated both the reduced-viologen signal and the 570 nm bleach signal similar to previously reported procedures.³¹ We extracted and averaged the ΔA signal over 660–690 nm for all samples.³⁷ The CdSe QD-only signal was then subtracted from the QD + viologen signal to extract signals due to the reduced viologen kinetics only.^{30,31} The reduced viologen kinetics were smoothed using a five-point moving average (The Supporting Information shows the raw data). We then extracted the kinetics at bleach maximum (570 nm) of the CdSe QD + viologen samples. We normalized the bleach kinetics with the pure reduced viologen kinetics at late times after the bleach signal was fully decayed ($> 10 \text{ ns}$ for the 1:1 viologen + QD sample, and $> 1 \text{ ns}$ for the higher ratios).³¹ We then subtracted the reduced viologen signal from the bleach signal to obtain the pure CdSe QD bleach signal for the CdSe QD + viologen samples. The pure CdSe QD bleach signal was then normalized such that its maximum value was equal to one. This procedure was performed for all four concentrations of both viologens. The lower initial amplitudes of the 570 nm bleach signal suggest that some ET occurs within the instrument response for the samples with higher viologen concentrations, but those early kinetics are convoluted with the instrument response. For this reason, all of our fits of the bleach kinetics start at 2 ps.

Kinetic Monte Carlo (kMC) Simulations. A kMC simulation was constructed to predict the QY of electron extraction by simulating the potential pathways of an excited electron using a previously established method for stochastic simulations.⁴⁷ The dependent variable of the simulation is the quantum yield of electron extraction ($\text{QY}_{\text{extraction}}$ eq 1).

$$\text{QY}_{\text{extraction}} = \frac{\text{\#electrons reaching destination}}{\text{\#initially excited electrons}} \quad (1)$$

A conduction band electron can either transfer with a rate constant of k_{ET} or recombine with its hole with a rate constant

k_0 . The probability of electron transfer to the viologen was determined by the quantum efficiency of electron transfer (QE_{ET}), that is the fraction of electrons which are transferred, calculated using eq 2 for MV^{2+} and eq 3 for $MVPO_3$

$$QE_{ET,MV} = \frac{N \times k_{ET}}{k_0 + N \times k_{ET}} \quad (2)$$

$$QE_{ET,MVPO_3} = \frac{N_f \times k_{ET,f} + N_l \times k_{ET,l}}{k_0 + N_f \times k_{ET,f} + N_l \times k_{ET,l}} \quad (3)$$

where N represents the number of viologens bound to the QD and is drawn separately each iteration from a Poisson distribution defined by the experimentally measured $\langle N \rangle$. The k_{ET} is determined by the experimental values obtained from kinetic modeling of TA spectroscopy data. In the case of $MVPO_3$ there is some fraction bound in both the face-on and ligand-like mode, with the $\langle N \rangle$ for each being the ITC-determined value and the k_{ET} for each mode as the experimental value from the kinetic fits. We approximate k_0 as the amplitude-weighted average rate constant from the multiexponential fit of the QD-only TA bleach kinetics (570 nm). If the electron is transferred to the viologen, it can either transfer back to recombine with the photoexcited hole with a rate constant of k_{BET} or be shuttled to the catalyst with a rate constant of $k_{shuttle}$. The probability of shuttling to the catalyst was determined by the quantum efficiency of electron shuttling ($QE_{shuttle}$), which is described in eq 4.

$$QE_{shuttle} = \frac{k_{shuttle}}{k_{BET} + k_{shuttle}} \quad (4)$$

where k_{BET} is the experimentally determined amplitude-weighted average rate constant for BET and $k_{shuttle}$ is the manually input independent variable. Each simulation was run for 1,000,000 excitations of the QD at a 1:1 viologen/QD molar ratio. The model assumes an excitation rate low enough that each excited electron has decayed before the next excitation occurs. A direct method was used for drawing pathways in each excitation.^{48,49}

A different kMC simulation was used to compare Poisson and binomial binding models and is described in the Supporting Information.

RESULTS AND DISCUSSION

With the aim of independently characterizing and controlling the binding of a molecular electron acceptor to CdSe QDs and the kinetics for ET and BET, we built on the established MV^{2+} platform. Reduced MV^{2+} ($MV^{+\bullet}$) has a strong absorption signal at energies below the CdSe QD band gap, allowing both the forward ET and BET reactions to be monitored by TA spectroscopy.^{50–52} Therefore, there is extensive literature precedent on characterizing charge transfer between CdSe QDs and MV^{2+} .^{29,31,32,51–54} In addition, the binding of MV^{2+} to CdS and CdSe QDs has been previously investigated by PL quenching combined with density functional theory.^{12,54,55} MV^{2+} was found to bind in a “face-on” configuration attributed to electrostatic adsorption of its positive bipyridine rings to anions (e.g., Se^{2-} , S^{2-}) on the QD surface (illustrated in Figure 1), at a distance of 2.9–3.3 Å from the QD surface. This strong interaction has made it difficult to tune ET behavior by derivatizing MV^{2+} . In prior work with a carboxylic acid functionalized viologen, varying the molecular linker length did

not significantly impact k_{ET} because transfer via the face-on interaction continued to dominate the ET.¹²

In an effort to enable both the surface attachment via a targeted binding group and the control over ET and BET behavior through tuning of molecular structure between the binding group and the bipyridine electron accepting moiety, we synthesized 1-methyl-1'-(2-phosphonoethyl)-[4,4'-bipyridine]-1,1'-dium dibromide ($MVPO_3$). $MVPO_3$ is a novel viologen derivative that shares the same ring structure as MV^{2+} but includes a phosphonic acid functional group (Figure 1). The characterization of $MVPO_3$ by infrared and nuclear magnetic resonance (NMR) spectroscopies and high-resolution mass spectrometry (HRMS) is described in the Methods section, and NMR spectra are shown in Figure S1. We use the abbreviation $MVPO_3$ because we expect that the phosphonic acid is deprotonated at neutral pH based on comparable phosphonic acids attached to positively charged groups.⁵⁶ We chose a phosphonate anchoring group because phosphonates are known to bind strongly to CdSe QD surfaces, even more strongly than carboxylates.^{17–19,57,58} We therefore hypothesized that $MVPO_3$ would allow the viologen to bind through the phosphonate linker in a “ligand-like” conformation (illustrated in Figure 1).

Spectroelectrochemistry measurements demonstrate that functionalization of MV^{2+} with a phosphonate does not significantly impact the absorbance spectrum of its reduced form, the radical cation ($MVPO_3^{+\bullet}$) (Figure 2A), showing a similar reduced-viologen feature as $MV^{+\bullet}$ (full spectra shown in Figure S2). Cyclic voltammetry (CV) measurements also reveal that MV^{2+} and $MVPO_3$ both have reduction potentials of -0.63 V vs SCE (Figure 2A inset). This comparison shows that the phosphonate functionalization does not substantially change the optical or electronic properties of the bipyridine moiety on $MVPO_3$ as compared to MV^{2+} , likely because the added phosphonate group is sufficiently separated from the redox-active bipyridine as to not have a significant impact on its energy levels.

The CdSe QDs used were synthesized using previously published methods.⁴³ An exchange from the native octadecylphosphonic acid to 3-mercaptopropionic acid (MPA) ligands was conducted to solubilize the QDs in H_2O and all experiments described below were conducted in Milli-Q pure water. The CdSe QDs were characterized by absorption and PL spectroscopies (Figure 2B). The QD first exciton peak is observed at 562 nm in the absorbance spectrum (Figure 2B), corresponding to a diameter of 3.5 nm,⁵⁹ which is corroborated by the diameter ($3.6 \text{ nm} \pm 0.8 \text{ nm}$, $N = 201$) determined by transmission electron microscopy (TEM) (Figures 2B inset and S3).

Characterization of Binding Thermodynamics with Isothermal Titration Calorimetry. To characterize the binding thermodynamics between CdSe QDs and MV^{2+} and $MVPO_3$, we turned to ITC. ITC has recently been shown to be a useful tool for examining nanocrystal–ligand binding^{23,58,60–69} and for qualitative assessment of interactions between QDs and molecular electron acceptors.^{70–73} ITC directly measures the heat evolved when species bind in solution and can be used to extract the dissociation equilibrium constant (K_d), which is the inverse of the binding equilibrium constant, the maximum number of bound species (n_{max}), and the enthalpy of binding (ΔH). The free energy (ΔG) and entropy (ΔS) of binding can also be calculated from the standard thermodynamic relationships.

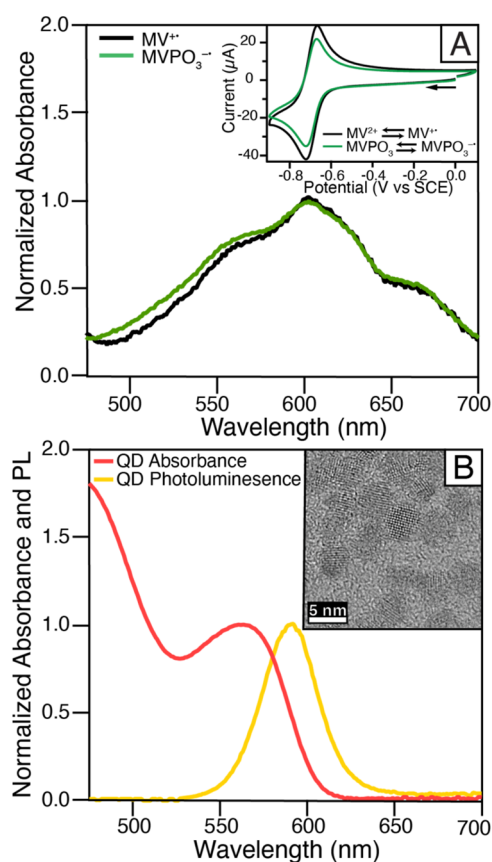


Figure 2. Characterization of viologens and CdSe QDs. (A) Normalized absorbance spectra of MV^{2+} (black) and $MVPO_3^{-\bullet}$ (green) in 0.25 M phosphate–NaOH buffer at pH 7.44. MV^{2+} and $MVPO_3^{-\bullet}$ were each electrochemically generated at -0.7 V vs Ag/AgCl. Inset A: CV of 2.5 mM MV^{2+} (black) and $MVPO_3^{-\bullet}$ (green) at 100 mV/s in aqueous 0.25 M phosphate–NaOH buffer at pH 7.44. (B) Normalized absorbance (red) and PL (yellow) spectra of aqueous 3.5 nm CdSe QDs. Inset B: Representative TEM of 3.5 nm CdSe QDs at 400k \times magnification.

ITC has several strengths: high sensitivity, generalizability to different types of binding without reliance on spectroscopic features, and the ability to deduce a full thermodynamic description of binding from a single experiment.²³ Compared to NMR spectroscopy, it requires less sample, it is better at distinguishing multiple binding modes, and is more general in what species can be probed.²³ In fact, MV^{2+} binding to QDs was found not to be amenable to NMR characterization because its NMR peaks were so broadened upon binding that they blended into the baseline.²² The sensitivity of ITC is a double-edged sword, because ITC detects all sources of enthalpy change upon injection, including solvent mixing and side reactions, which may make it difficult to isolate only the signals from the heat of binding. In the **Methods** section, we describe the control experiments and precautions we undertook to extract reliable ITC data.

Figure 3 shows the ITC binding characterization for MV^{2+} and $MVPO_3$. The positive peaks in the MV^{2+} thermogram (Figure 3A) indicate exothermic (enthalpically favorable) binding. The sharp, single peaks suggest that the binding reaches equilibrium fairly quickly after each injection and that there is a single binding mechanism without side processes releasing significant heat. Individual replicates for MV^{2+} binding were consistent (Figure S4). The thermogram for

$MVPO_3$ (Figure 3B) is more complex—while the peaks are still predominantly exothermic they do contain an endothermic component, which is most visible in the peaks between 1000 and 1300 s. This behavior is consistent with the presence of two distinct binding modes between CdSe QDs and $MVPO_3$, one of which is exothermic and the other endothermic. The negative (endothermic) peak consistently appears after the positive one, suggesting that the endothermic binding process is slower to reach equilibrium than the exothermic one. The endothermic peaks are not observable at low titration ratios, likely because the initial exothermic signal is so strong it obscures the other mode. However, the exothermic mode also appears to saturate at lower mole ratios than the endothermic mode, allowing the endothermic signal to be revealed at higher concentrations. Despite this complex shape, the data was consistent across replicates (Figure S5) and had clean controls (Figure S6).

Figure 3C shows the integrated isotherm for the MV^{2+} titration. It fits well to the Langmuir–Wiseman isotherm model, which assumes independent adsorption events to identical sites until the binding sites are saturated. This model is well established in the literature for the adsorption of organic ligands to NC surfaces,^{23,60,68} and yields values for K_d , n_{max} , and ΔH (Table 1). The K_d of $32 \pm 2 \mu M$ is comparable to that estimated by PL quenching for other viologen–QD systems.^{22,74} It indicates relatively strong bonding and is in the same order of magnitude as K_d values for many covalently bound ligands, suggesting a strong attraction between CdSe QDs and MV^{2+} .^{67,68} We found n_{max} to be 22 ± 2 . The extracted value of ΔH is $-20 \pm 1 \text{ kJ mol}^{-1}$, which is in the same order of magnitude as many previously studied QD–ligand systems.^{58,62,67}

The two binding modes of $MVPO_3$ that are observed in the thermogram (Figure 3B) are more apparent in the integrated isotherm (Figure 3D). The formation of the peak at 17:1 $MVPO_3/QD$ ratio requires the existence of both an endothermic and an exothermic process.⁵⁸ To fit the data, we used a sum of two Langmuir–Wiseman isotherms, one exothermic and one endothermic, each corresponding to a different attachment mode. Figure 3D shows the overall binding model as a solid line that passes through the data as well as the two component isotherms. The exothermic component is simulated as the dashed line “Fit 1” and the endothermic component is simulated as the dotted line “Fit 2”. For the exothermic component, we obtain fit constants of $K_d = 99 \pm 2 \mu M$, $n_{max} = 11 \pm 1$, and $\Delta H = -47 \pm 6 \text{ kJ mol}^{-1}$. For the endothermic mode we get $K_d = 10 \pm 8 \mu M$, $n_{max} = 18.1 \pm 0.7$, and $\Delta H = 11 \pm 7 \text{ kJ mol}^{-1}$.

Given that MV^{2+} only experiences face-on binding and has a negative ΔH , we hypothesize that the exothermic component of the $MVPO_3$ thermograms reflects a similar face-on mode. We observe a higher K_d (meaning weaker binding) and lower n_{max} in the face-on binding of $MVPO_3$ than in MV^{2+} (Table 1). This may be due to increased steric hindrance from the presence of the relatively bulky phosphonate group. Electrostatic repulsions with the negative charges on the phosphonate and MPA surface ligands may also play a role. The difference in ΔH may also be attributable to these interactions.

We assign the endothermic component of the CdSe QD– $MVPO_3$ ITC to a ligand-like binding mode shown in Figure 1. For this component, we observe stronger binding (lower K_d) than for the face-on binding in $MVPO_3$ or in MV^{2+} . This is consistent with our expectation that the covalent bond of the

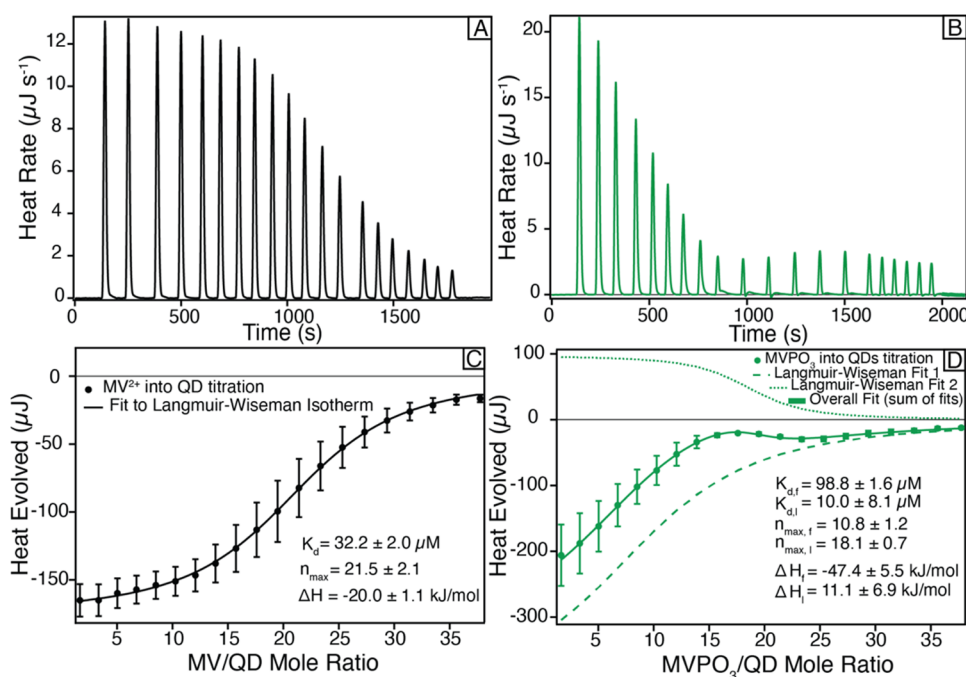


Figure 3. ITC characterization of CdSe QD-viologen binding. (A, B) Representative thermogram of 29 μM aqueous solutions of QDs titrated with (A) MV^{2+} and (B) MVPO_3 . (C) Integrated isotherm of MV^{2+} titrated into QDs best fit to the Langmuir–Wiseman isotherm model, indicating one set of identical independent binding sites. Data shown are the average of three replicates with error bars indicating one standard deviation (individual trials are shown in Figure S4). (D) Integrated isotherm of MVPO_3 titrated into QDs with best fit to a sum of two Langmuir–Wiseman isotherms (solid line). Each component of the two-component isotherm is shown as a dashed (exothermic) or dotted (endothermic) line. Data shown are the average of three replicates with error bars indicating one standard deviation (individual trials in Figure S5).

Table 1. Thermodynamic Parameters from ITC Data Fitting^a

sample and binding mode	K_d (μM)	n_{max} (# bound per QD)	ΔH (kJ mol^{-1})	ΔG (kJ mol^{-1})	ΔS ($\text{J mol}^{-1} \text{K}^{-1}$)
MV^{2+} (only face-on)	32 ± 2	22 ± 2	-20 ± 1	-25.6 ± 0.2	19 ± 4
MVPO_3 face-on	99 ± 2	11 ± 1	-47 ± 6	-22.86 ± 0.04	-80 ± 20
MVPO_3 ligand-like	10 ± 8	18.1 ± 0.7	11 ± 7	-29 ± 3	130 ± 30

^aAnalysis was conducted on the average of three replicates. Uncertainties are 95% confidence intervals from fit. K_d , n_{max} , and ΔH are fit directly, whereas ΔG and ΔS are derived from the directly fit parameters using their thermodynamic relations.

ligand-like mode would be stronger than the face-on electrostatic adsorption. We obtain a ΔH of $11 \pm 7 \text{ kJ mol}^{-1}$, indicating the binding is weakly endothermic. Endothermic binding has been observed in prior literature^{58,75,76} and could occur here due to rearrangement of the solvation shell upon binding,⁷⁷ reconstruction of the QD surface,^{58,78} disruption to the existing MPA ligand layer due to interactions with the comparatively large viologen molecule,^{61,62} or changes to the protonation state of MVPO_3 upon binding to the QD. The endothermicity suggests that the spontaneous binding of MVPO_3 in its ligand-like conformation is driven by the entropy of creating a mixed ligand layer. Calculated entropy values (Table 1) are consistent with this, revealing the ΔS of the MVPO_3 ligand-like mode to be $130 \text{ J mol}^{-1} \text{K}^{-1}$, which is the only ITC component measured to have a significant positive entropy. As we show in the next section, the ITC data provides input parameters for analyzing the ET kinetics probed by TA spectroscopy, allowing us to determine the ET rate constant for each binding mode.

We have considered modeling the phosphonate binding mode as a ligand exchange,^{23,67} rather than adsorption but multiple observations conflict with this interpretation so we decided against it. Face-on binding occurs primarily through Se^{2-} ions, meaning we do not expect it to directly compete

with the existing MPA ligands or with ligand-like binding for sites.⁵⁵ The ligand-like mode binds through Cd^{2+} , which is also where MPA is thought to bind,⁷⁹ suggesting that this process could be a competitive ligand exchange. However, such a mechanism is not consistent with the data. The relatively low n_{max} suggests that only a relatively small fraction of the surface Cd atoms can be occupied by MVPO_3 , despite the fact that the K_d indicates binding that is quite strong. Prior work has shown that exchanging a phosphonic acid for MPA is thermodynamically favorable.⁶⁷ Thus, if MVPO_3 were replacing MPA ligands, the result would be a relatively high K_d but it would eventually be able to displace most MPA at high concentrations. Instead, our data shows a strong binding, which saturates abruptly at ~ 18 ligands/QD; this is more consistent with a process where MVPO_3 is binding to Cd^{2+} sites that are already under-coordinated owing to incomplete MPA surface coverage. Importantly, as described later in the text, TA data for the QD– MVPO_3 system cannot be described well with a ligand exchange model either.

We additionally considered the possibility that MVPO_3 binds through the phosphonate and bipyridine rings simultaneously, facilitated by flexibility along the carbon linker, as has been previously observed in perylene diimide acceptors.⁸⁰ However, the difference in n_{max} between the face-on and

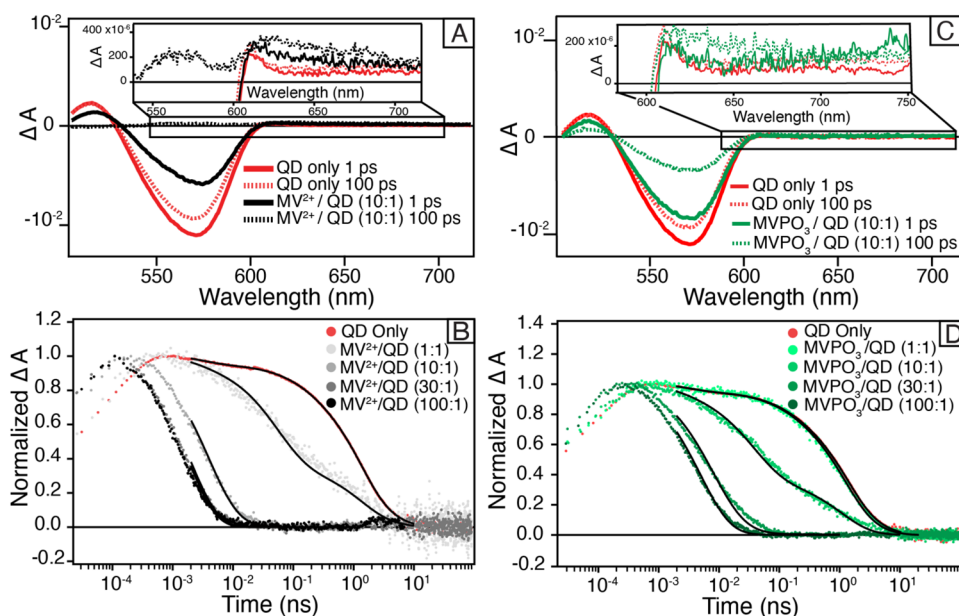


Figure 4. TA spectroscopy data of aqueous CdSe QDs with MV^{2+} and $MVPO_3$. (A) TA spectra of CdSe QDs alone (red) and CdSe QDs with MV^{2+}/QD at a 10:1 ratio (black) at 1 ps (solid lines) and 100 ps (dotted lines) after 480 nm pump excitation. The inset shows a zoomed in region to visualize the MV^{2+} feature. (B) Kinetics of the bleach decay at 570 nm for CdSe QDs alone (red) and CdSe QDs with four different concentrations of MV^{2+} (gray–black) normalized at their maximum value. The data are shown as dots and best fits to eq 5 are shown as solid black lines. (C) TA spectra of CdSe QDs alone (red) and CdSe QDs with $MVPO_3/QD$ at a 10:1 ratio (green) at 1 ps (solid lines) and 100 ps (dotted lines) after pulsed 480 nm laser excitation. The inset shows a zoomed in region to visualize the $MVPO_3^-$ feature. (D) Kinetics of the bleach decay at 570 nm for CdSe QDs alone (red) and CdSe QDs with four different concentrations of $MVPO_3$ (light green–dark green) normalized at their maximum. The data are shown as dots and best fits to eq 6 are shown as solid black lines.

ligand-like binding modes, as well as the different time scales of their occurrence, indicates that they are not correlated. Given that the model of two independent binding modes fits the ITC data, and the TA data later in the text, our results do not justify invoking a third binding mode that couples the two existing modes, or other similarly complex scenarios. Additionally, we do not see any evidence of aggregation-induced spectral changes or ET slowing at high $MVPO_3$ concentrations, which were observed in the perylenediimide system.⁸⁰

In summary, for MV^{2+} binding we observe one binding mode, consistent with the previously established face-on binding. For $MVPO_3$ we observe two binding modes, which we hypothesize are due to a face-on binding mode and a ligand-like binding mode through the phosphonate group. The fraction of molecules bound in each of the binding modes is determined by their respective dissociation constants, which are shown later for use in the analysis of the TA data.

Electron Transfer from CdSe QDs to MV^{2+} . After using ITC to examine the binding landscape, we set out to understand how these binding phenomena impact ET to MV^{2+} and $MVPO_3$ as detected by transient absorption (TA) spectroscopy. Figure 4A,B shows the results of the TA measurements for ET from CdSe QDs to MV^{2+} . UV–visible absorbance spectra of the corresponding samples, before and after TA spectroscopy experiments, are shown in Figure S7. The samples were excited at 480 nm to minimize direct excitation of MV^{2+} (Figure S2). The pump power was chosen to minimize the formation of multiexcitons and the samples were stirred continuously under rigorously air-free conditions (see Methods for details). Figure 4A shows ΔA spectra of aqueous CdSe QDs with 0:1 (red) and 10:1 (black) MV^{2+}/QD ratios at 1 ps (solid) and 100 ps (dotted) after excitation. We observe three main features in the CdSe QD-only spectrum: a

bleach at 570 nm associated with electron occupancy of the CdSe QD conduction band, a positive peak at 610 nm associated with hot carrier cooling, and a weak, broad feature from ≈ 600 nm to the red edge of our detectable signal (≈ 750 nm) associated with trapped holes.^{5,24,33} In samples containing MV^{2+} (black lines) the MV^{2+} feature appears as an induced absorption at 500–700 nm (Figure 4A). The bleach feature is by far the strongest. It provides information about the excited-state lifetime of the CdSe QDs, and reports on electron relaxation processes, such as electron–hole recombination and electron trapping.^{4,5,30,81} We therefore use it to quantitatively analyze ET kinetics below. In the analysis of the kinetics, the overlapping contributions of the QD and MV^{2+} signals were accounted for as described in the Methods section.

In the CdSe QD-only sample in Figure 4A, the bleach decay is slow compared to the samples where MV^{2+} is present; after 100 ps the peak intensity is still above 80% of its original value. The addition of MV^{2+} introduces ET as another pathway by which the electron can leave the conduction band which competes with the intrinsic CdSe QD relaxation processes.^{4,5,34} The transfer to MV^{2+} is quite fast; at 1 ps the bleach peak for the sample with MV^{2+} is ca. 50% that of the CdSe QD alone, and by 100 ps the bleach has completely decayed (Figure 4A). The decay of the CdSe QD bleach and rise of the MV^{2+} feature occur on the same time scale (Figure S8). This indicates that the significant shortening of the QD electron decay time is due to ET to MV^{2+} . This ultrafast ET from CdSe QDs to MV^{2+} has been observed previously and has been attributed to the intimate binding in the face-on mode.^{30,32,52,54,82}

In Figure 4B, we plot the intensity of the 570 nm bleach signal as a function of pump–probe delay for CdSe QD samples with 5 different MV^{2+}/QD molar ratios: 0:1 (CdSe QD-only), 1:1, 10:1, 30:1, and 100:1, with the CdSe QD

concentration held constant at 10.6 μM . Some of the bleach decay occurs within the instrument response function (IRF) as shown in Figure S9. Hence, we normalized the bleach intensity at the maximum value of each kinetic trace (≈ 1 ps).^{50,51,53,83} Although the MV^{2+} signal is minuscule at 570 nm compared to the strength of the QD bleach, its intensity increases as the QD bleach decreases (both owing to ET), so we rigorously removed the MV^{2+} contribution to the 570 nm bleach following previously established procedures³¹ as described in the Methods section.

For quantitative analysis of the ET kinetics, we start with the assumption that all changes to the CdSe QD electron decay are due to ET and not other pathways, as justified above.³⁴ Therefore, the decay of the QD– MV^{2+} samples can be described as a product of QD-only decay (which includes electron–hole recombination and electron trapping) and decay owing to ET to MV^{2+} .⁸⁴ We only seek to analyze this second factor in the product, thus the QD-only decay was best fit with a sum of four exponentials, as described previously,²² and was not interpreted further (eq S1 and Table S1). This factor accounts for all electron decay processes internal to the QD, including electron–hole recombination and electron trapping, and was then held constant for all the samples containing MV^{2+} .^{22,37} To model the decay component due to ET, we multiply the QD-only factor by a model that has been well established for ET from QDs to molecules, including viologens.^{22,28,37,85} The model assumes a Poisson distribution of bound MV^{2+} and is expressed as

$$S(t)_{\text{ET,MV}} = \exp[\langle N \rangle \times (e^{-k_{\text{ET}}t} - 1)] \quad (5)$$

where $S_{\text{ET,MV}}$ is the TA decay component due to ET, $\langle N \rangle$ is the average number of MV^{2+} molecules bound to each QD, and t is the time since excitation. The Poisson distribution of acceptors arises because the probability of an acceptor being bound is independent of whether one is already bound.^{74,85} The choice of this model is discussed further in Section S10 and compared to a binomial distribution in Figure S10.

The Poisson-distribution model for ET has two variable parameters, the average number of viologens bound ($\langle N \rangle$) and k_{ET} . Allowing both parameters to freely vary can lead to difficulties deconvoluting the impact of each parameter on the observed rate and they can be correlated.²² Instead, we calculate $\langle N \rangle$ at every concentration based on the information derived from ITC (eqs S2–S5) and fix this parameter (Table 2). This leaves k_{ET} as the only adjustable parameter. As shown in Figure 4B, this constrained Poisson model fits the data quite well and the best fit gives an intrinsic k_{ET} of $(2.4 \pm 0.7) \times 10^{10} \text{ s}^{-1}$. This value is the average of k_{ET} obtained at the four MV^{2+} concentrations, which are shown in Table S2. It is comparable to those observed in prior literature.^{22,32,51,86} Incidentally, letting both k_{ET} and $\langle N \rangle$ float gives similar best-fit values for all

Table 2. $\langle N \rangle$ Predicted by ITC Data for Each Viologen Mode

viologen/QD ratio	$\langle N \rangle$		
	MV^{2+} (only face-on)	MVPO_3 face-on	MVPO_3 ligand-like
1:1	0.87	0.057	0.89
10:1	8.2	0.86	8.3
30:1	17	5.2	16
100:1	21	9.6	18

parameters (Figure S11 and Table S3). Overall, our analysis of ET in CdSe QD– MV^{2+} , constrained by the binding parameters from ITC, yields results that are similar to the literature precedent. This validates our methodology and provides a jumping-off point for understanding the impact of the more complex binding landscape for MVPO_3 on its ET profile.

Electron Transfer from CdSe QDs to MVPO_3 . To characterize ET kinetics from CdSe QDs to MVPO_3 and compare them with those for MV^{2+} , we carried out analogous TA measurements at the same concentrations. Figure 4C shows the ΔA spectra for aqueous CdSe QDs with MVPO_3 at 0:1 and 10:1 MVPO_3 to CdSe QD molar ratios. The spectra contain the same features as observed for the MV^{2+} + CdSe QD data shown in Figure 4A. Even before kinetic analysis, it is clear that the impact of MVPO_3 on the CdSe QD kinetics is smaller than that of MV^{2+} . The 570 nm bleach is not quenched as strongly for MVPO_3 ; unlike with MV^{2+} , there is still some bleach signal remaining at 100 ps. Similarly, the $\text{MVPO}_3^{\bullet-}$ feature is slower to grow in and of smaller magnitude for MVPO_3 than for MV^{2+} (Figures 4C and 5). Both these observations suggest that ET from CdSe QDs is slower to MVPO_3 than to MV^{2+} .

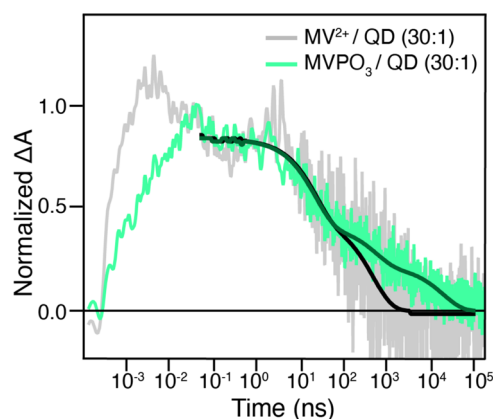


Figure 5. Kinetics of the reduced-viologen feature (averaged over 660–690 nm). MV^{2+}/QD (30:1) data is shown as light gray and double exponential fit is shown as black. $\text{MVPO}_3^{\bullet-}/\text{QD}$ (30:1) data is shown as light green and triple exponential fit is shown as dark green. All fitting was done on the raw data shown in Figure S16. The kinetic traces shown here were smoothed using a five-point moving average to reduce noise in the visualization.

The ET kinetics from CdSe QDs to MVPO_3 were obtained in the same fashion as for MV^{2+} . The TA signal was extracted at 570 nm and the CdSe QD-only decay was fit to four exponentials (Figure 4D). For our kinetic analysis we again assume that the binding of MVPO_3 does not impact the intrinsic QD kinetics and only adds an ET pathway. To justify this assumption, we show that the decay of the 570 nm bleach and the rise of the $\text{MVPO}_3^{\bullet-}$ occur together, confirming that ET to MVPO_3 is the primary process by which the conduction band electron decays (Figure S12). Given that ITC reveals two distinct modes by which MVPO_3 can bind to the CdSe QDs and that the data in Figure 4D cannot be fit with the model in eq 5 (Figure S13 and Table S4), we model the data with two distinct ET pathways, one for each binding mode. We assume that the population of QD–acceptor species, in each binding mode, can be described with a Poisson distribution. This

scenario has been considered previously, resulting in the derivation of eq 6, which has been used when there were two different, independent, pathways of electron decay, each with a Poisson distribution of acceptors.^{34,87,88}

$$S(t)_{\text{ET,MVPO}_3} = \exp[\langle N_f \rangle \times (e^{-k_{\text{ET},f} \times t} - 1)] \\ \times \exp[\langle N_l \rangle \times (e^{-k_{\text{ET},l} \times t} - 1)] \quad (6)$$

where $\langle N_f \rangle$ and $\langle N_l \rangle$ refer to the average number of MVPO₃ bound in the face-on and ligand-like conformation respectively, and $k_{\text{ET},f}$ and $k_{\text{ET},l}$ are the rate constants for ET to MVPO₃ bound in the face-on and ligand-like mode, respectively. We determine $\langle N \rangle$ for each mode from the ITC data (Table 2 and eqs S6–S12) and keep these values fixed in data fitting.

This model fits the TA data remarkably well (Figure 4D), leading us to conclude that adding more complex scenarios with additional adjustable parameters is not justified. Our analysis reveals that $k_{\text{ET},f} = (1.5 \pm 1.0) \times 10^{10} \text{ s}^{-1}$ and $k_{\text{ET},l} = (3 \pm 4) \times 10^7 \text{ s}^{-1}$. Consistent with observations from ITC, the value of $k_{\text{ET},f}$ is within the error of the value obtained for the CdSe QD–MV²⁺ complex. This supports the assignment of the minor binding mode in ITC as the face-on mode and suggests that functionalization of MV²⁺ does not significantly impact ET through the face-on binding conformation. More interestingly, $k_{\text{ET},l}$ is 3 orders of magnitude slower than k_{ET} observed for the face-on binding mode. We hypothesize that the much slower rate constant for ligand-like binding is caused by the increased distance between the surface of the CdSe QD and the bipyridine ring, which is the electron accepting part of the molecule, when compared to the intimate contact in the face-on mode.^{3,12,54,89–92} Density functional theory has estimated that face-on adsorption binding results in 2.9–3.3 Å between the QD surface and MV²⁺ molecule, which is shorter than the length of the linker in MVPO₃ which we estimate to be around 6 Å.^{54,55} Ultimately, the reason that overall ET to MVPO₃ is slower than to MV²⁺ is that a significant fraction of molecules are bound in the ligand-like conformation, which exhibits a slower rate constant for ET. It is unlikely that this slow component of ET would be attributable to collisional ET with unbound MVPO₃, as MV²⁺ has a greater unbound fraction based on ITC (Table 2), but does not show this slower component of ET.

As an additional control, we collected TA data in the presence of ethylphosphonic acid, which may bind through the phosphonate similar to MVPO₃ but cannot accept electrons. This molecule did not significantly change the dynamics of the CdSe QD bleach decay at early times that are most relevant to ET (Figure S14). Phosphonate adsorption may contribute some lifetime lengthening owing to electron trap passivation at later times (after ET), as seen in Figure S14, which would make $k_{\text{ET},l}$ somewhat of an underestimate of the true value. However, the data does not justify adding more parameters to the model so we use the value from the fit to eq 6 as our best estimate of the $k_{\text{ET},l}$.

We also tested a model for ET to MVPO₃ that assumes that the ligand-like binding requires a ligand exchange instead of adsorption. In this method, K_{dl} is not a true dissociation constant, but instead is an effective constant (K_{observed}) that can be used to approximate a ligand exchange equilibrium constant (K_{ex}) by the relation: $K_{\text{ex}} = n_{\text{max}} \times [\text{QD}]_{\text{tot}} / K_{\text{observed}}$.^{23,58,67} This model fails to fit trends in the TA data, offering further evidence that our model of MVPO₃ binding to exposed surface

sites is a more accurate picture of this system than an exchange of MPA for MVPO₃ (Figure S15 and Table S5).

Overall, the success of using binding information from ITC as fixed parameters to analyze the TA in concert with the reasonable values of k_{ET} obtained for the different binding modes lend confidence to our approach to revealing how synthetic modification of the electron acceptor impacts ET kinetics.

Charge Recombination in CdSe QD-Viologen Complexes. While the efficiency of forward ET is important for potential photochemical applications, so is the lifetime of the resulting charge-separated state(s). The time scale for BET—the time it takes for the electron to transfer from the reduced acceptor molecule back to the oxidized CdSe QD—needs to be long enough to accumulate the stoichiometric charge required for fuel formation, which may be difficult under conditions such as low light intensity, poor absorbance per NC, and large number of electron-accepting catalysts.^{2,50,93–96} Even for single electron-accepting molecules like viologens, which have been used as electron shuttles,^{38,97} increasing charge-separated state lifetime is critical to achieving the desired reactivity. Given that MVPO₃ exhibits a slower rate of ET than MV²⁺ due to the increased distance of the bipyridine from the CdSe QD surface, we expect that BET will also be slowed.

To study the kinetics of BET, we examined the TA signal for the reduced-viologen feature of MV^{+•} and MVPO₃^{•-}. Figure 5 shows the extracted kinetics for the aqueous 30:1 viologen/QD samples. The decay of the reduced-viologen feature for MV²⁺ was best fit to a double exponential (eq S17) from which we extracted an amplitude-weighted average lifetime, $\langle \tau_{\text{cs}} \rangle$ (eq S18), of $0.51 \pm 0.02 \mu\text{s}$ (full fit values in Table S6).³⁷ Due to its short duration, the early (<50 ps) decay does not contribute meaningfully to the average lifetime—if we include this fast component in the data fit, we still get $\langle \tau_{\text{cs}} \rangle = 0.51 \pm 0.02 \mu\text{s}$. To facilitate comparison with the MVPO₃^{•-} signal, we start the fit when its rise is complete, at 45 ps. The MVPO₃^{•-} sample appears to decay similarly to MV^{+•} at earlier times (<10 ns) but has a component that extends out to longer times. We hypothesize that, similar to ET, the BET process has two components associated with the two binding modes. The kinetics associated with the face-on mode are similar for the two molecules while the ligand-like mode potentially has different kinetics. We therefore fit the decay of the QD–MVPO₃^{•-} sample to a triple exponential. The first two time constants were held at values extracted from the data for MV^{+•}, while the third was allowed to float. By allowing all three amplitudes to float, a time constant for the slow component was best fit to a value of $19.4 \pm 1.0 \mu\text{s}$, resulting in $\langle \tau_{\text{cs}} \rangle = 19.0 \pm 0.2 \mu\text{s}$. This is a 37-fold increase in charge-separation-state lifetime as compared to conventional MV²⁺. This result shows that alteration of the binding geometry can be used to tune both ET and BET. The slowing of both forward and reverse ET rate constants is consistent with our hypothesis that the separation distance between CdSe QD and the bipyridine group is a key driver of the rate of interfacial electron transfer in this system, and that by increasing that separation distance, both directions of charge transfer are slowed.

Interplay of ET and BET Kinetics in Light-Driven Chemistry. With both ET and BET slowed down in the ligand-like binding mode of MVPO₃, it is not immediately obvious whether this is better or worse for reactions that use the electrons transferred to viologens than the face-on-binding

of MV^{2+} and the associated relatively fast ET and BET. MV^{2+} has been demonstrated as an efficient redox shuttle to move electrons from a photoabsorber, such as NCs, to another destination, such as a catalyst,^{38,97} and here we consider such a reaction. To address the interplay of the ET and BET rates in these systems, we built a kinetic Monte Carlo (kMC) simulation that simulated the quantum yield (QY) of electron extraction—that is the fraction of excited electrons in the QD that are shuttled to the intended destination—for QDs combined with MV^{2+} and $MVPO_3$. Figure 6A shows a scheme

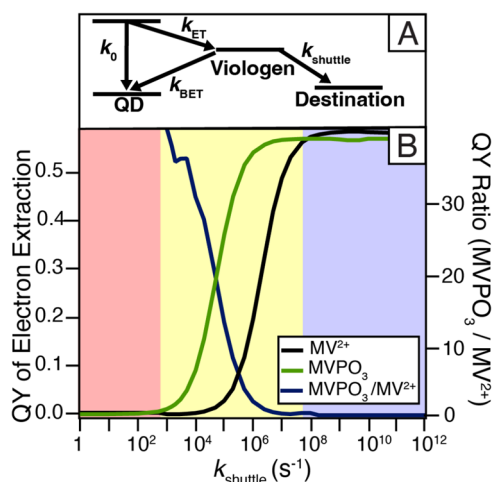


Figure 6. Kinetic Monte Carlo (kMC) simulation of a hypothetical electron shuttling process. (A) Schematic of kinetic processes studied by the simulation. (B) Results of a kMC simulation studying QY of electron extraction (left axis) vs k_{shuttle} for a 1:1 ratio of viologen/QD for both MV^{2+} (black) and $MVPO_3$ (green). To better visualize the fractional improvement, we also plot the ratio of QYs obtained with $MVPO_3$ and MV^{2+} (dark blue trace, right axis). We observe three regions in the k_{shuttle} dependence: k_{shuttle} is too slow for either viologen to get a significant QY (red), k_{shuttle} is competitive with k_{BET} and thus a slower BET rate constant improves QY (yellow), and k_{shuttle} is sufficiently large to outcompete BET in both molecules and thus the ET efficiency is the driver for QY (blue).

of the processes simulated. The simulation inputs draw from our experimental results wherever possible: MV^{2+} is bound in a Poisson distribution with an $\langle N \rangle$ described in Table 2 and a k_{ET} from TA modeling, $MVPO_3$ has fractions bound as both face-on and ligand-like where the $\langle N \rangle$ and k_{ET} for each mode are similarly derived from the experimental data. The electron–hole recombination rate constant (k_0) and k_{BET} are modeled as single rate constants using the amplitude weighted average of their respective multiexponential fits, and k_{shuttle} is an independent variable. The simulation assumes a sufficiently low excitation rate that only one electron is excited at a time and recombines with a hole before the next excitation.

Figure 6B shows the results of the simulation over a range of potential rate constants for the process of shuttling the electron from the viologen to its next destination (k_{shuttle}) for a 1:1 ratio of viologen/QD. The simulation reveals that $MVPO_3$ has a significantly higher QY of electron extraction when k_{shuttle} is relatively competitive with k_{BET} , approximately 10^3 – 10^7 s^{-1} . The extension of the charge separated lifetimes significantly improves its ability to shuttle electrons to a catalyst before BET occurs, and this effect is strong enough to outweigh the impact of receiving electrons less efficiently. In fact, the difference in the forward ET efficiency between the two viologens is quite

minimal. For samples with QDs and MV^{2+} , we calculate that 58.2% of electrons are transferred (although for each MV^{2+} bound, ET is 100% efficient, many QDs do not have any MV^{2+} bound at this mixing ratio). For $MVPO_3$ this forward efficiency is only slightly worse: 56.3% of electrons are transferred in the overall ensemble (92.4% in the QDs with $MVPO_3$ bound) because even this slower ET is competitive with other electron relaxation pathways. For very small values of k_{shuttle} (<1000 s^{-1}) the QY is ≈ 0 for both viologens as neither reduced form lives long enough to shuttle the electron before BET occurs. However, for k_{shuttle} in the moderate range, $MVPO_3$ has a significantly higher QY of extraction than MV^{2+} , over 30 times improvement at the slower end of the moderate range and approaching 1 as k_{shuttle} increases. For very high values of k_{shuttle} ($>10^8$) the BET rate also ceases to matter, as nearly all electrons that reach the viologen will be shuttled; in this regime, MV^{2+} does act as a minimally more efficient electron shuttle than $MVPO_3$ because it accepts electrons from the QD just slightly more efficiently. Note that the simulation accounts for the small fraction of $MVPO_3$ that is bound in the face-on configuration, showing that perfect selectivity for one binding mode is not necessary to achieve significant performance improvements. To better visualize performance improvements we plot the ratio of the QY of electron extraction for $MVPO_3/MV^{2+}$ (Figure 6, dark blue trace, right axis). These results show that the balance of ET and BET kinetics obtained with $MVPO_3$ is beneficial over a wide range of reaction scenarios. Overall, the BET contributes more strongly to the difference observed between the two viologens, as the forward ET efficiencies are not as significantly different.

CONCLUSIONS

We synthesized a novel viologen derivative containing a phosphonic acid for binding to CdSe QDs with similar electrochemical properties as MV^{2+} . A ligand-like binding mode via the phosphonate group was identified using ITC and found to be stronger than the face-on binding of the bipyridine group, but not sufficiently selective to be the exclusive binding mode. Ultrafast TA spectroscopy data, analyzed using binding information from ITC, showed that the rate constants for photoinduced interfacial ET from CdSe QDs to surface-anchored MV^{2+} or $MVPO_3$ bound via the face-on mode were similar, while the ET rate constant for surface-anchored $MVPO_3$ bound via the ligand-like mode was 3 orders of magnitude slower. Recombination via BET to the oxidized CdSe QD was also slower from $MVPO_3^{\bullet-}$ as compared to $MV^{\bullet+}$, extending the lifetime of the charge-separated state by more than 30-fold. Using numerical simulations, we showed that the ET and BET kinetics with $MVPO_3$ increase the quantum yield of reactions that use the electron on the bipyridine group when their rate constants are in the ranges of 10^3 – 10^7 s^{-1} . Our work contributes to the development of NC–molecule donor–acceptor systems with controlled charge transfer kinetics by revealing detailed binding information that allows for the determination of ET rate constants for distinct attachment geometries and by predicting the impacts of those kinetics on downstream reactions that use the photogenerated electrons.

ASSOCIATED CONTENT

Supporting Information

The Supporting Information is available free of charge at <https://pubs.acs.org/doi/10.1021/acs.jpcc.5c00740>.

Full characterization of viologens and QDs; ITC replicates and controls; details of calculations used to extract $\langle N \rangle$; and further details of TA spectroscopy modeling with alternative models (PDF)

AUTHOR INFORMATION

Corresponding Author

Gordana Dukovic – Department of Chemistry, University of Colorado Boulder, Boulder, Colorado 80309-0215, United States; Materials Science and Engineering and Renewable and Sustainable Energy Institute, University of Colorado Boulder, Boulder, Colorado 80309-0215, United States; orcid.org/0000-0001-5102-0958; Email: gordana.dukovic@colorado.edu

Authors

- Olivia F. Bird** – Department of Chemistry, University of Colorado Boulder, Boulder, Colorado 80309-0215, United States; orcid.org/0000-0001-8836-2687
- Kenneth M. Drbohlav** – Department of Chemistry, Fort Lewis College, Durango, Colorado 81301, United States
- Evan K. Gowdy** – Department of Chemistry, Fort Lewis College, Durango, Colorado 81301, United States
- Faith A. Flinkingshelt** – Department of Chemistry, University of California, Irvine, Irvine, California 92697, United States; orcid.org/0009-0007-9238-9613
- Lauren M. Pellows** – Department of Chemistry, University of Colorado Boulder, Boulder, Colorado 80309-0215, United States; orcid.org/0000-0002-1088-1898
- Benjamin F. Hammel** – Materials Science and Engineering, University of Colorado Boulder, Boulder, Colorado 80309-0215, United States; orcid.org/0000-0002-9155-9875
- Bradley W. Layne** – Department of Chemistry, University of California, Irvine, Irvine, California 92697, United States
- Shane Ardo** – Department of Chemistry, University of California, Irvine, Irvine, California 92697, United States; Department of Chemical and Biomolecular Engineering and Department of Materials Science and Engineering, University of California, Irvine, California 92697, United States; orcid.org/0000-0001-7162-6826
- Jenny Y. Yang** – Department of Chemistry, University of California, Irvine, Irvine, California 92697, United States; Physical Sciences Division, Physical and Computational Sciences Directorate, Pacific Northwest National Laboratory, Richland, Washington 99354, United States; orcid.org/0000-0002-9680-8260
- Kenneth A. Miller** – Department of Chemistry, Fort Lewis College, Durango, Colorado 81301, United States; orcid.org/0000-0002-0316-3396

Complete contact information is available at: <https://pubs.acs.org/10.1021/acs.jpcc.5c00740>

Author Contributions

◆K.M.D. and E.K.G. contributed equally to this work.

Notes

The authors declare no competing financial interest.

ACKNOWLEDGMENTS

This research was supported as part of Ensembles of Photosynthetic Nanoreactors (EPN), an Energy Frontier Research Center funded by the U.S. Department of Energy, Office of Science under Award Number DE-SC0023431.

O.F.B. and B.F.H. acknowledge support from the National Science Foundation through the Graduate Research Fellowship Program (NSF-GRFP) under Grant No. DGE 2040434. We thank the Shared Instruments Pool (RRID: SCR_018986) of the Department of Biochemistry at the University of Colorado Boulder for the use of its ITC and Annette Erbs for training and assistance with experiment design. High Resolution Mass Spectrometry data was taken at University of Colorado Boulder Central Analytical Laboratory and Mass Spectrometry Facility (CAL) (RRID:SCR_018992) by Chris Ebmeier and Naifu Zhang. TEM images were collected at the Facility for Electron Microscopy of Materials at the University of Colorado Boulder (CU FEMM, RRID: SCR_019306). We thank Andrew Greytak for helpful ITC discussions and Madison Jilek and Skylar Sherman for training and assistance with TA spectroscopy data collection and interpretation.

REFERENCES

- (1) Liu, J.; Ren, Y.-Y.; Wu, J.; Xia, W.; Deng, B.-Y.; Wang, F. Hybrid Artificial Photosynthetic Systems Constructed Using Quantum Dots and Molecular Catalysts for Solar Fuel Production: Development and Advances. *J. Mater. Chem. A* **2021**, *9* (35), 19346–19368.
- (2) Burke, R.; Bren, K. L.; Krauss, T. D. Semiconductor Nanocrystal Photocatalysis for the Production of Solar Fuels. *J. Chem. Phys.* **2021**, *154* (3), No. 030901.
- (3) Harris, R. D.; Homan, S. B.; Kodaimati, M.; He, C.; Nepomnyashchii, A. B.; Swenson, N. K.; Lian, S.; Calzada, R.; Weiss, E. A. Electronic Processes within Quantum Dot-Molecule Complexes. *Chem. Rev.* **2016**, *116* (21), 12865–12919.
- (4) Shulenberger, K. E.; Jilek, M. R.; Sherman, S. J.; Hohman, B. T.; Dukovic, G. Electronic Structure and Excited State Dynamics of Cadmium Chalcogenide Nanorods. *Chem. Rev.* **2023**, *123* (7), 3852–3903.
- (5) Zhu, H.; Yang, Y.; Wu, K.; Lian, T. Charge Transfer Dynamics from Photoexcited Semiconductor Quantum Dots. *Annu. Rev. Phys. Chem.* **2016**, *67* (1), 259–281.
- (6) Wen, F.; Yang, J.; Zong, X.; Ma, B.; Wang, D.; Li, C. Photocatalytic H₂ Production on Hybrid Catalyst System Composed of Inorganic Semiconductor and Cobaloximes Catalysts. *J. Catal.* **2011**, *281* (2), 318–324.
- (7) Wang, F.; Wang, W.-G.; Wang, X.-J.; Wang, H.-Y.; Tung, C.-H.; Wu, L.-Z. A Highly Efficient Photocatalytic System for Hydrogen Production by a Robust Hydrogenase Mimic in an Aqueous Solution. *Angew. Chem., Int. Ed.* **2011**, *50* (14), 3193–3197.
- (8) Han, Z.; Qiu, F.; Eisenberg, R.; Holland, P. L.; Krauss, T. D. Robust Photogeneration of H₂ in Water Using Semiconductor Nanocrystals and a Nickel Catalyst. *Science* **2012**, *338* (6112), 1321–1324.
- (9) Huang, J.; Mulfort, K. L.; Du, P.; Chen, L. X. Photodriven Charge Separation Dynamics in CdSe/ZnS Core/Shell Quantum Dot/Cobaloxime Hybrid for Efficient Hydrogen Production. *J. Am. Chem. Soc.* **2012**, *134* (40), 16472–16475.
- (10) Lian, S.; Kodaimati, M. S.; Dolzhnikov, D. S.; Calzada, R.; Weiss, E. A. Powering a CO₂ Reduction Catalyst with Visible Light through Multiple Sub-Picosecond Electron Transfers from a Quantum Dot. *J. Am. Chem. Soc.* **2017**, *139* (26), 8931–8938.
- (11) Bi, Q.-Q.; Wang, J.-W.; Lv, J.-X.; Wang, J.; Zhang, W.; Lu, T.-B. Selective Photocatalytic CO₂ Reduction in Water by Electrostatic Assembly of CdS Nanocrystals with a Dinuclear Cobalt Catalyst. *ACS Catal.* **2018**, *8* (12), 11815–11821.
- (12) Morris-Cohen, A. J.; Peterson, M. D.; Frederick, M. T.; Kamm, J. M.; Weiss, E. A. Evidence for a Through-Space Pathway for Electron Transfer from Quantum Dots to Carboxylate-Functionalized Viologens. *J. Phys. Chem. Lett.* **2012**, *3* (19), 2840–2844.
- (13) Huang, J.; Huang, Z.; Yang, Y.; Zhu, H.; Lian, T. Multiple Exciton Dissociation in CdSe Quantum Dots by Ultrafast Electron

- Transfer to Adsorbed Methylene Blue. *J. Am. Chem. Soc.* **2010**, *132* (13), 4858–4864.
- (14) Zhu, H.; Song, N.; Lian, T. Controlling Charge Separation and Recombination Rates in CdSe/ZnS Type I Core–Shell Quantum Dots by Shell Thicknesses. *J. Am. Chem. Soc.* **2010**, *132* (42), 15038–15045.
- (15) Boulesbaa, A.; Huang, Z.; Wu, D.; Lian, T. Competition between Energy and Electron Transfer from CdSe QDs to Adsorbed Rhodamine B. *J. Phys. Chem. C* **2010**, *114* (2), 962–969.
- (16) Boulesbaa, A.; Issac, A.; Stockwell, D.; Huang, Z.; Huang, J.; Guo, J.; Lian, T. Ultrafast Charge Separation at CdS Quantum Dot/Rhodamine B Molecule Interface. *J. Am. Chem. Soc.* **2007**, *129* (49), 15132–15133.
- (17) Knauf, R. R.; Lennox, J. C.; Dempsey, J. L. Quantifying Ligand Exchange Reactions at CdSe Nanocrystal Surfaces. *Chem. Mater.* **2016**, *28* (13), 4762–4770.
- (18) De Roo, J. The Surface Chemistry of Colloidal Nanocrystals Captured by Organic Ligands. *Chem. Mater.* **2023**, *35* (10), 3781–3792.
- (19) Gomes, R.; Hassinen, A.; Szczygiel, A.; Zhao, Q.; Vantomme, A.; Martins, J. C.; Hens, Z. Binding of Phosphonic Acids to CdSe Quantum Dots: A Solution NMR Study. *J. Phys. Chem. Lett.* **2011**, *2* (3), 145–152.
- (20) Hens, Z. Ligands on Nanocrystal Surfaces, the ¹H Nuclear Magnetic Resonance Fingerprint. *Acc. Chem. Res.* **2023**, *56* (12), 1623–1633.
- (21) Donakowski, M. D.; Godbe, J. M.; Sknepnek, R.; Knowles, K. E.; de la Cruz, M. O.; Weiss, E. A. A Quantitative Description of the Binding Equilibria of Para-Substituted Aniline Ligands and CdSe Quantum Dots. *J. Phys. Chem. C* **2010**, *114* (51), 22526–22534.
- (22) Morris-Cohen, A. J.; Frederick, M. T.; Cass, L. C.; Weiss, E. A. Simultaneous Determination of the Adsorption Constant and the Photoinduced Electron Transfer Rate for a CdS Quantum Dot–Viologen Complex. *J. Am. Chem. Soc.* **2011**, *133* (26), 10146–10154.
- (23) Greytak, A. B.; Abiodun, S. L.; Burrell, J. M.; Cook, E. N.; Jayaweera, N. P.; Islam, M. M.; Shaker, A. E. Thermodynamics of Nanocrystal–Ligand Binding through Isothermal Titration Calorimetry. *Chem. Commun.* **2022**, *58* (94), 13037–13058.
- (24) Klimov, V. I. Optical Nonlinearities and Ultrafast Carrier Dynamics in Semiconductor Nanocrystals. *J. Phys. Chem. B* **2000**, *104* (26), 6112–6123.
- (25) Hyun, B.-R.; Bartnik, A. C.; Lee, J.-K.; Imoto, H.; Sun, L.; Choi, J. J.; Chujo, Y.; Hanrath, T.; Ober, C. K.; Wise, F. W. Role of Solvent Dielectric Properties on Charge Transfer from PbS Nanocrystals to Molecules. *Nano Lett.* **2010**, *10* (1), 318–323.
- (26) Tvrdy, K.; Frantsuzov, P. A.; Kamat, P. V. Photoinduced Electron Transfer from Semiconductor Quantum Dots to Metal Oxide Nanoparticles. *Proc. Natl. Acad. Sci. U.S.A.* **2011**, *108* (1), 29–34.
- (27) Zhu, H.; Yang, Y.; Hyeon-Deuk, K.; Califano, M.; Song, N.; Wang, Y.; Zhang, W.; Prezhdo, O. V.; Lian, T. Auger-Assisted Electron Transfer from Photoexcited Semiconductor Quantum Dots. *Nano Lett.* **2014**, *14* (3), 1263–1269.
- (28) Sadhu, S.; Tachiya, M.; Patra, A. A Stochastic Model for Energy Transfer from CdS Quantum Dots/Rods (Donors) to Nile Red Dye (Acceptors). *J. Phys. Chem. C* **2009**, *113* (45), 19488–19492.
- (29) Harris, C.; Kamat, P. V. Photocatalysis with CdSe Nanoparticles in Confined Media: Mapping Charge Transfer Events in the Subpicosecond to Second Timescales. *ACS Nano* **2009**, *3* (3), 682–690.
- (30) Zhu, H.; Lian, T. Enhanced Multiple Exciton Dissociation from CdSe Quantum Rods: The Effect of Nanocrystal Shape. *J. Am. Chem. Soc.* **2012**, *134* (27), 11289–11297.
- (31) Zhu, H.; Song, N.; Rodríguez-Córdoba, W.; Lian, T. Wave Function Engineering for Efficient Extraction of up to Nineteen Electrons from One CdSe/CdS Quasi-Type II Quantum Dot. *J. Am. Chem. Soc.* **2012**, *134* (9), 4250–4257.
- (32) Scholz, F.; Dworak, L.; Matylitsky, V. V.; Wachtveitl, J. Ultrafast Electron Transfer from Photoexcited CdSe Quantum Dots to Methylviologen. *ChemPhysChem* **2011**, *12* (12), 2255–2259.
- (33) Klimov, V. I. Spectral and Dynamical Properties of Multiexcitons in Semiconductor Nanocrystals. *Annu. Rev. Phys. Chem.* **2007**, *58* (1), 635–673.
- (34) Utterback, J. K.; Wilker, M. B.; Brown, K. A.; King, P. W.; Eaves, J. D.; Dukovic, G. Competition between Electron Transfer, Trapping, and Recombination in CdS Nanorod–Hydrogenase Complexes. *Phys. Chem. Chem. Phys.* **2015**, *17* (8), 5538–5542.
- (35) Leng, H.; Loy, J.; Amin, V.; Weiss, E. A.; Pelton, M. Electron Transfer from Single Semiconductor Nanocrystals to Individual Acceptor Molecules. *ACS Energy Lett.* **2016**, *1* (1), 9–15.
- (36) Meyer, H. M.; Chen, J.; Loomis, R. A.; Buhro, W. E. Facet-Specific Electron Transfer in Pseudo-Two-Dimensional Wurtzite Cadmium Selenide Nanocrystals. *J. Phys. Chem. C* **2023**, *127* (37), 18506–18517.
- (37) Zhao, F.; Li, Q.; Han, K.; Lian, T. Mechanism of Efficient Viologen Radical Generation by Ultrafast Electron Transfer from CdS Quantum Dots. *J. Phys. Chem. C* **2018**, *122* (30), 17136–17142.
- (38) Zhu, H.; Song, N.; Lv, H.; Hill, C. L.; Lian, T. Near Unity Quantum Yield of Light-Driven Redox Mediator Reduction and Efficient H₂ Generation Using Colloidal Nanorod Heterostructures. *J. Am. Chem. Soc.* **2012**, *134* (28), 11701–11708.
- (39) Ballabio, M.; Cánovas, E. Electron Transfer at Quantum Dot–Metal Oxide Interfaces for Solar Energy Conversion. *ACS Nanosci. Au* **2022**, *2* (5), 367–395.
- (40) Wu, K.; Liang, G.; Shang, Q.; Ren, Y.; Kong, D.; Lian, T. Ultrafast Interfacial Electron and Hole Transfer from CsPbBr₃ Perovskite Quantum Dots. *J. Am. Chem. Soc.* **2015**, *137* (40), 12792–12795.
- (41) Katir, N.; Majoral, J. P.; El Kadib, A.; Caminade, A.-M.; Bousmina, M. Molecular and Macromolecular Engineering with Viologens as Building Blocks: Rational Design of Phosphorus–Viologen Dendritic Structures. *Eur. J. Org. Chem.* **2012**, *2012* (2), 269–273.
- (42) Rountree, E. S.; McCarthy, B. D.; Eisenhart, T. T.; Dempsey, J. L. Evaluation of Homogeneous Electrocatalysts by Cyclic Voltammetry. *Inorg. Chem.* **2014**, *53* (19), 9983–10002.
- (43) Manthiram, K.; Beberwyck, B. J.; Talapin, D. V.; Alivisatos, A. P. Seeded Synthesis of CdSe/CdS Rod and Tetrapod Nanocrystals. *J. Visualized Exp.* **2013**, No. 82, No. e50731.
- (44) Brown, K. A.; Wilker, M. B.; Boehm, M.; Dukovic, G.; King, P. W. Characterization of Photochemical Processes for H₂ Production by CdS Nanorod–[FeFe] Hydrogenase Complexes. *J. Am. Chem. Soc.* **2012**, *134* (12), 5627–5636.
- (45) Schindelin, J.; Arganda-Carreras, I.; Frise, E.; Kaynig, V.; Longair, M.; Pietzsch, T.; Preibisch, S.; Rueden, C.; Saalfeld, S.; Schmid, B.; et al. Fiji: An Open-Source Platform for Biological-Image Analysis. *Nat. Methods* **2012**, *9* (7), 676–682.
- (46) Homer, M. K.; Larson, H. C.; Dixon, G. J.; Miura-Stempel, E.; Armstrong, N. R.; Cossairt, B. M. Extremely Long-Lived Charge Donor States Formed by Visible Irradiation of Quantum Dots. *ACS Nano* **2024**, *18* (35), 24591–24602.
- (47) Voter, A. F. Introduction to the Kinetic Monte Carlo Method. In *Radiation Effects in Solids*; Sickafus, K. E.; Kotomin, E. A.; Uberuaga, B. P., Eds.; NATO Science Series; Springer: Dordrecht, Netherlands, 2007; Vol. 235, pp 1–23.
- (48) Gillespie, D. T. A General Method for Numerically Simulating the Stochastic Time Evolution of Coupled Chemical Reactions. *J. Comput. Phys.* **1976**, *22* (4), 403–434.
- (49) Bortz, A. B.; Kalos, M. H.; Lebowitz, J. L. A New Algorithm for Monte Carlo Simulation of Ising Spin Systems. *J. Comput. Phys.* **1975**, *17* (1), 10–18.
- (50) Kobosko, S. M.; DuBose, J. T.; Kamat, P. V. Perovskite Photocatalysis. Methyl Viologen Induces Unusually Long-Lived Charge Carrier Separation in CsPbBr₃ Nanocrystals. *ACS Energy Lett.* **2020**, *5* (1), 221–223.

- (51) Sekhar, M. C.; Paul, S.; De, A.; Samanta, A. An Ultrafast Transient Absorption Study of Charge Separation and Recombination Dynamics in CdSe QDs and Methyl Viologen: Dependence on Surface Stoichiometry. *ChemistrySelect* **2018**, *3* (9), 2675–2682.
- (52) Wang, Y.-F.; Wang, H.-Y.; Li, Z.-S.; Zhao, J.; Wang, L.; Chen, Q.-D.; Wang, W.-Q.; Sun, H.-B. Electron Extraction Dynamics in CdSe and CdSe/CdS/ZnS Quantum Dots Adsorbed with Methyl Viologen. *J. Phys. Chem. C* **2014**, *118* (31), 17240–17246.
- (53) Dworak, L.; Matylitsky, V. V.; Breus, V. V.; Braun, M.; Basché, T.; Wachtveitl, J. Ultrafast Charge Separation at the CdSe/CdS Core/Shell Quantum Dot/Methylviologen Interface: Implications for Nanocrystal Solar Cells. *J. Phys. Chem. C* **2011**, *115* (10), 3949–3955.
- (54) Chen, J.; Wu, K.; Rudshiteyn, B.; Jia, Y.; Ding, W.; Xie, Z.-X.; Batista, V. S.; Lian, T. Ultrafast Photoinduced Interfacial Proton Coupled Electron Transfer from CdSe Quantum Dots to 4,4'-Bipyridine. *J. Am. Chem. Soc.* **2016**, *138* (3), 884–892.
- (55) Peterson, M. D.; Jensen, S. C.; Weinberg, D. J.; Weiss, E. A. Mechanisms for Adsorption of Methyl Viologen on CdS Quantum Dots. *ACS Nano* **2014**, *8* (3), 2826–2837.
- (56) Freedman, L. D.; Doak, G. O. The Preparation And Properties Of Phosphonic Acids. *Chem. Rev.* **1957**, *57* (3), 479–523.
- (57) Dhaene, E.; Pokratath, R.; Aalling-Frederiksen, O.; Jensen, K. M. Ø.; Smet, P. F.; De Buysser, K.; De Roo, J. Monoalkyl Phosphinic Acids as Ligands in Nanocrystal Synthesis. *ACS Nano* **2022**, *16* (5), 7361–7372.
- (58) Gee, M. Y.; Shen, Y.; Greytak, A. B. Isothermal Titration Calorimetry Resolves Sequential Ligand Exchange and Association Reactions in Treatment of Oleate-Capped CdSe Quantum Dots with Alkylphosphonic Acid. *J. Phys. Chem. C* **2020**, *124* (43), 23964–23975.
- (59) Jasieniak, J.; Smith, L.; van Embden, J.; Mulvaney, P.; Califano, M. Re-Examination of the Size-Dependent Absorption Properties of CdSe Quantum Dots. *J. Phys. Chem. C* **2009**, *113* (45), 19468–19474.
- (60) Williams, E. S.; Major, K. J.; Tobias, A.; Woodall, D.; Morales, V.; Lippincott, C.; Moyer, P. J.; Jones, M. Characterizing the Influence of TOPO on Exciton Recombination Dynamics in Colloidal CdSe Quantum Dots. *J. Phys. Chem. C* **2013**, *117* (8), 4227–4237.
- (61) Elimelech, O.; Aviv, O.; Oded, M.; Banin, U. A Tale of Tails: Thermodynamics of CdSe Nanocrystal Surface Ligand Exchange. *Nano Lett.* **2020**, *20* (9), 6396–6403.
- (62) Elimelech, O.; Aviv, O.; Oded, M.; Peng, X.; Harries, D.; Banin, U. Entropy of Branching Out: Linear versus Branched Alkylthiol Ligands on CdSe Nanocrystals. *ACS Nano* **2022**, *16* (3), 4308–4321.
- (63) Brewer, A. S.; Calvin, J. J.; Alivisatos, A. P. Impact of Uniform Facets on the Thermodynamics of Ligand Exchanges on Colloidal Quantum Dots. *J. Phys. Chem. C* **2023**, *127* (21), 10270–10281.
- (64) Calvin, J. J.; Ben-Moshe, A.; Curling, E. B.; Brewer, A. S.; Sedlak, A. B.; Kaufman, T. M.; Alivisatos, A. P. Thermodynamics of the Adsorption of Cadmium Oleate to Cadmium Sulfide Quantum Dots and Implications of a Dynamic Ligand Shell. *J. Phys. Chem. C* **2022**, *126* (30), 12958–12971.
- (65) Calvin, J. J.; O'Brien, E. A.; Sedlak, A. B.; Balan, A. D.; Alivisatos, A. P. Thermodynamics of Composition Dependent Ligand Exchange on the Surfaces of Colloidal Indium Phosphide Quantum Dots. *ACS Nano* **2021**, *15* (1), 1407–1420.
- (66) Ravi, V.; Binz, J. M.; Rioux, R. M. Thermodynamic Profiles at the Solvated Inorganic–Organic Interface: The Case of Gold–Thiolate Monolayers. *Nano Lett.* **2013**, *13* (9), 4442–4448.
- (67) Dunlap, J. H.; Jayaweera, N. P.; Pellechia, P. J.; Greytak, A. B. Competitive Anionic Exchange of Thiolate Ligands onto Aqueous Phosphonate-Capped Quantum Dots. *J. Phys. Chem. C* **2022**, *126* (41), 17635–17646.
- (68) Shen, Y.; Tan, R.; Gee, M. Y.; Greytak, A. B. Quantum Yield Regeneration: Influence of Neutral Ligand Binding on Photophysical Properties in Colloidal Core/Shell Quantum Dots. *ACS Nano* **2015**, *9* (3), 3345–3359.
- (69) Elimelech, O.; Oded, M.; Harries, D.; Banin, U. Spontaneous Patterning of Binary Ligand Mixtures on CdSe Nanocrystals: From Random to Janus Packing. *ACS Nano* **2023**, *17* (6), 5852–5860.
- (70) Bharadwaj, K.; Choudhary, H.; Hazra, S.; Ghosh, S. Study of Interfacial Charge Transfer from an Electron Rich Organic Molecule to CdTe Quantum Dot by Using Stern-Volmer and Stochastic Kinetic Models. *ChemPhysChem* **2020**, *21* (5), 415–422.
- (71) Wang, Y.-Y.; Xiang, X.; Yan, R.; Liu, Y.; Jiang, F.-L. Förster Resonance Energy Transfer from Quantum Dots to Rhodamine B As Mediated by a Cationic Surfactant: A Thermodynamic Perspective. *J. Phys. Chem. C* **2018**, *122* (2), 1148–1157.
- (72) Dey, S.; Das, B.; Voggu, R.; Nag, A.; Sarma, D. D.; Rao, C. N. R. Interaction of CdSe and ZnO Nanocrystals with Electron-Donor and -Acceptor Molecules. *Chem. Phys. Lett.* **2013**, *556*, 200–206.
- (73) Mishra, K.; Das, A.; Ghosh, S. Ultrafast Interfacial Electron Transfer from Graphene Quantum Dot to 2,4-Dinitrotoluene. *J. Phys. Chem. C* **2021**, *125* (18), 9638–9645.
- (74) Morris-Cohen, A. J.; Vasilenko, V.; Amin, V. A.; Reuter, M. G.; Weiss, E. A. Model for Adsorption of Ligands to Colloidal Quantum Dots with Concentration-Dependent Surface Structure. *ACS Nano* **2012**, *6* (1), 557–565.
- (75) Limo, M. J.; Perry, C. C. Thermodynamic Study of Interactions Between ZnO and ZnO Binding Peptides Using Isothermal Titration Calorimetry. *Langmuir* **2015**, *31* (24), 6814–6822.
- (76) Abiodun, S. L.; Gee, M. Y.; Greytak, A. B. Combined NMR and Isothermal Titration Calorimetry Investigation Resolves Conditions for Ligand Exchange and Phase Transformation in CsPbBr₃ Nanocrystals. *J. Phys. Chem. C* **2021**, *125* (32), 17897–17905.
- (77) Duff, M. R.; Howell, E. E. Thermodynamics and Solvent Linkage of Macromolecule–Ligand Interactions. *Methods* **2015**, *76*, 51–60.
- (78) Boles, M. A.; Ling, D.; Hyeon, T.; Talapin, D. V. The Surface Science of Nanocrystals. *Nat. Mater.* **2016**, *15* (2), 141–153.
- (79) Owen, J. The Coordination Chemistry of Nanocrystal Surfaces. *Science* **2015**, *347* (6222), 615–616.
- (80) Cadena, D. M.; Sowa, J. K.; Cotton, D. E.; Wight, C. D.; Hoffman, C. L.; Wagner, H. R.; Boette, J. T.; Raulerson, E. K.; Iverson, B. L.; Rossky, P. J.; Roberts, S. T. Aggregation of Charge Acceptors on Nanocrystal Surfaces Alters Rates of Photoinduced Electron Transfer. *J. Am. Chem. Soc.* **2022**, *144* (49), 22676–22688.
- (81) He, S.; Li, Q.; Jin, T.; Lian, T. Contributions of Exciton Fine Structure and Hole Trapping on the Hole State Filling Effect in the Transient Absorption Spectra of CdSe Quantum Dots. *J. Chem. Phys.* **2022**, *156* (5), No. 054704.
- (82) Matylitsky, V. V.; Dworak, L.; Breus, V. V.; Basché, T.; Wachtveitl, J. Ultrafast Charge Separation in Multiexcited CdSe Quantum Dots Mediated by Adsorbed Electron Acceptors. *J. Am. Chem. Soc.* **2009**, *131* (7), 2424–2425.
- (83) DuBose, J. T.; Kamat, P. V. Surface Chemistry Matters. How Ligands Influence Excited State Interactions between CsPbBr₃ and Methyl Viologen. *J. Phys. Chem. C* **2020**, *124* (24), 12990–12998.
- (84) Utterback, J. K.; Wilker, M. B.; Mulder, D. W.; King, P. W.; Eaves, J. D.; Dukovic, G. Quantum Efficiency of Charge Transfer Competing against Nonexponential Processes: The Case of Electron Transfer from CdS Nanorods to Hydrogenase. *J. Phys. Chem. C* **2019**, *123* (1), 886–896.
- (85) Tachiya, M. Kinetics of Quenching of Luminescent Probes in Micellar Systems. II. *J. Chem. Phys.* **1982**, *76* (1), 340–348.
- (86) Harris, C.; Kamat, P. V. Photocatalytic Events of CdSe Quantum Dots in Confined Media. Electrode Behavior of Coupled Platinum Nanoparticles. *ACS Nano* **2010**, *4* (12), 7321–7330.
- (87) Knowles, K. E.; McArthur, E. A.; Weiss, E. A. A Multi-Timescale Map of Radiative and Nonradiative Decay Pathways for Excitons in CdSe Quantum Dots. *ACS Nano* **2011**, *5* (3), 2026–2035.
- (88) Huang, T.; Koh, T. T.; Schwan, J.; Tran, T. T.-T.; Xia, P.; Wang, K.; Mangolini, L.; Tang, M. L.; Roberts, S. T. Bidirectional Triplet Exciton Transfer between Silicon Nanocrystals and Perylene. *Chem. Sci.* **2021**, *12* (19), 6737–6746.

(89) Wilker, M. B.; Utterback, J. K.; Greene, S.; Brown, K. A.; Mulder, D. W.; King, P. W.; Dukovic, G. Role of Surface-Capping Ligands in Photoexcited Electron Transfer between CdS Nanorods and [FeFe] Hydrogenase and the Subsequent H₂ Generation. *J. Phys. Chem. C* **2018**, *122* (1), 741–750.

(90) Asbury, J. B.; Hao, E.; Wang, Y.; Lian, T. Bridge Length-Dependent Ultrafast Electron Transfer from Re Polypyridyl Complexes to Nanocrystalline TiO₂ Thin Films Studied by Femtosecond Infrared Spectroscopy. *J. Phys. Chem. B* **2000**, *104* (50), 11957–11964.

(91) Beane, G.; Boldt, K.; Kirkwood, N.; Mulvaney, P. Energy Transfer between Quantum Dots and Conjugated Dye Molecules. *J. Phys. Chem. C* **2014**, *118* (31), 18079–18086.

(92) Koole, R.; Liljeroth, P.; de Mello Donegá, C.; Vanmaekelbergh, D.; Meijerink, A. Electronic Coupling and Exciton Energy Transfer in CdTe Quantum-Dot Molecules. *J. Am. Chem. Soc.* **2006**, *128* (32), 10436–10441.

(93) Hisatomi, T.; Kubota, J.; Domen, K. Recent Advances in Semiconductors for Photocatalytic and Photoelectrochemical Water Splitting. *Chem. Soc. Rev.* **2014**, *43* (22), 7520–7535.

(94) Wu, K.; Zhu, H.; Liu, Z.; Rodríguez-Córdoba, W.; Lian, T. Ultrafast Charge Separation and Long-Lived Charge Separated State in Photocatalytic CdS–Pt Nanorod Heterostructures. *J. Am. Chem. Soc.* **2012**, *134* (25), 10337–10340.

(95) Tkaczibson, K.; Ardo, S. Numerical Monte Carlo Simulations of Charge Transport across the Surface of Dye and Cocatalyst Modified Spherical Nanoparticles under Conditions of Pulsed or Continuous Illumination. *Sustainable Energy Fuels* **2019**, *3* (6), 1573–1587.

(96) Chen, H.-Y.; Ardo, S. Direct Observation of Sequential Oxidations of a Titania-Bound Molecular Proxy Catalyst Generated through Illumination of Molecular Sensitizers. *Nat. Chem.* **2018**, *10* (1), 17–23.

(97) Du, P.; Schneider, J.; Jarosz, P.; Eisenberg, R. Photocatalytic Generation of Hydrogen from Water Using a Platinum(II) Terpyridyl Acetylide Chromophore. *J. Am. Chem. Soc.* **2006**, *128* (24), 7726–7727.